Supplementary Materials for

Beyond Murray's Law: Resistance Matching Principle for Optimal Fluid Transport in Hierarchical Nanomaterials

Jian Cao[1,2], Xueting Deng[1,2], Zehui Liu[1,2], Xiaoyan Ji[3], Aatto Laaksonen[1,3,4,5], Francesca Mocci[6], Xin Feng[1], Yudan Zhu[1,2], Xiang Ling[7], Xiaohua Lu[1,2*]

[1] State Key Laboratory of Materials-Oriented and Chemical Engineering, Nanjing Tech University, Nanjing 211816, China

[2] Suzhou laboratory, Suzhou 215125, China

[3] Energy Engineering, Division of Energy Science, Luleå University of Technology, 97187, Luleå, Sweden

[4] Department of Chemistry, Arrhenius Laboratory, Stockholm University, Stockholm 10691, Sweden

[5] Center of Advanced Research in Bionanoconjugates and Biopolymers, Petru Poni Institute of Macromolecular Chemistry, Iasi 700469, Romania

[6] Department of Chemical and Geological Sciences, University of Cagliari, Monserrato 09042, Italy

[7] Jiangsu Key Laboratory of Process Enhancement and Energy Equipment Technology, School of Mechanical and Power Engineering, Nanjing Tech University, Nanjing 211816, China

*Corresponding author. Email: xhlu@njtech.edu.cn

Contents

Supplementary texts

S1. Derivation of original Murray's law: Poiseuille flow

For the laminar flow in the cylindrical channel, original Murray's law was derived based on the Hagen-Poiseuille (HP) equation as shown in **Eq. (S1)**, in which the pre-assumption of interfacial slip-negligibility should be satisfied, only the viscous resistance R_η of fluid flow was considered to describe the volumetric flow rate Q:

$$Q = \frac{\Delta P}{R_\eta} = \Delta P \cdot \frac{\pi r^4 \rho}{8\eta l} \tag{S1}$$

where ΔP is the pressure difference along the pore channels, r and l are the radius and length of the pore channels, respectively. **Eq. (S1)** is obtained based on the no-slip boundary condition, i.e., the fluid boundary velocity $v(\pm r) = 0$ in the fluid velocity distribution $v(z)$ as plotted in **Fig. 2a**. The optimization function under the constraint of a certain volume V can be written by introducing a Lagrange multiplier λ_1 as:

$$f = Q\Delta P - \lambda_1 V = Q\Delta P - \lambda_1 \pi r^2 l \tag{S2}$$

Taking the partial derivative of the optimization parameter r for this Lagrange function, the extreme value can be obtained when the partial derivative is equal to zero:

$$\frac{\partial\left[Q\Delta P - \lambda_1 \pi r^2 l\right]}{\partial r} = 0 \tag{S3}$$

Then, **Eq. (S3)** can be expressed as:

$$\frac{\Delta P}{l} = \sqrt{\frac{4\eta\lambda}{\rho r^2}} \tag{S4}$$

Substituting **Eq. (S4)** into **Eq. (S1)**, the optimization result can be obtained:

$$Q = \frac{\pi}{\sqrt{16\eta/\lambda\rho}} r^3 = kr^3 \tag{S5}$$

According to the mass conservation, the mass flows in parent pipes are equal to that in all children pipes, then the optimised results can be written as **Eq. (S6)**:

$$\frac{1}{\sqrt{\eta_0/\rho_0}} r_0^3 = \frac{1}{\sqrt{\eta_i/\rho_i}} \sum_1^{N_i} r_i^3 \tag{S6}$$

where N_i is the number of children pipes connected to a parent tube, and subscript i represents the level of children tubes. When another pre-assumption of fluid homogeneity holds, i.e., the density ρ and the viscosity η of fluids in parent pipes are equal to those in children tubes, **Eq. (S6)** can be simplified as the original Murray's law as shown in **Eq. (S7)**:

$$r_0^3 = \sum_1^{N_i} r_i^3 \tag{S7}$$

S2. Derivation of original Murray's law: mass diffusion

For mass diffusion, the basic transport equation can be described as:

$$Q_d = D_e \pi r^2 \frac{\Delta c}{l} \tag{S8}$$

where D_e is the diffusion coefficient. Δc is the concentration difference, which is the driving force for the mass diffusion. Similar to the above derivation, the optimization function can be written by introducing the Lagrange multiplier λ_2 as:

$$\frac{\partial\left[Q_d \Delta c - \lambda_2 \pi r^2 l\right]}{\partial r} = 0 \tag{S9}$$

Then, **Eq. (S9)** can be expressed as:

$$\Delta c = l \cdot \sqrt{\frac{\lambda_2}{D_e}} \tag{S10}$$

Substituting **Eq. (S10)** into **Eq. (S8)**, the optimized results can be described as:

$$Q_d = \pi \sqrt{\lambda D_e} r^2 = k r^2 \tag{S11}$$

$$k_0 r_0^2 = \sum_{i=1}^{N} k_i r_i^2 \tag{S12}$$

Eq. (S12) can be derived when the diffusion coefficient in **Eq. (S11)** is constant. Based on similar transport equations, identical results appear for heat transfer, ionic transfer, and electronic transfer. Therefore, a general formula for the original Murray's law can be written as:

$$r_0^{\alpha} = \sum_{1}^{N_i} r_i^{\alpha} \tag{S13}$$

where $\alpha = 3$ for laminar flow of liquids, and $\alpha = 2$ for mass diffusion of gases, which serves to provide a quantitative criterion for optimal hierarchical structures.

S3. Re-derived Murray's law at nanoscale

The slip-modified Hagen-Poiseuille (HP) equation can be used to describe the mass transport with nanoscale effects, incorporating interfacial slip and fluid heterogeneity:

$$Q_{slip} = \frac{\Delta P \pi r^4 \rho_{avg}}{8\eta l} + \frac{\Delta P \pi r^3 \rho_{avg} b}{2\eta l} \tag{S14}$$

Similar to the derivation of original Murray's law, the optimization function under the constraint of a certain volume V can be written by introducing a Lagrange multiplier λ_3 as:

$$f = Q_{slip}\Delta P - \lambda_3 V = Q_{slip}\Delta P - \lambda_3 \pi r^2 l \tag{S15}$$

Taking the partial derivative of the optimization parameter r for this Lagrange function, the extreme value can be obtained when the partial derivative is equal to zero:

$$\frac{\partial\left[Q_{slip}\Delta P - \lambda_3 \pi r^2 l\right]}{\partial r} = 0 \tag{S16}$$

Then, **Eq. (S16)** can be expressed as:

$$\frac{\Delta P}{l} = \sqrt{\frac{4\eta_{avg}\lambda_3}{\rho_{avg} r^2 \left(1+3b/r\right)}} \tag{S17}$$

Substituting **Eq. (S17)** into **Eq. (S14)**, the optimised result can be obtained:

$$Q_{slip} = \frac{\pi}{4} \cdot \sqrt{\frac{\lambda_3 \rho_{avg} \left(1+4b/r\right)^2}{\eta_{avg}\left(1+3b/r\right)}} r^3 \tag{S18}$$

According to the mass conservation, the mass flow rates of fluid in parent pipes are equal to those in children pipes:

$$\sqrt{\frac{\rho_{avg,0}\left(1+4b/r_0\right)^2}{\eta_{avg,0}\left(1+3b/r_0\right)}} r_0^3 = \sqrt{\frac{\rho_{avg,i}\left(1+4b/r_i\right)^2}{\eta_{avg,i}\left(1+3b/r_i\right)}} \sum\nolimits_1^{N_i} r_i^3 \tag{S19}$$

S4. Derivation of resistance matching principle

Linear non-equilibrium thermodynamics (NET) provides a unified framework to model different transport phenomena including flow and diffusion, which can be described as the relationship between the flux J and driving force X[1, 2, 3]:

$$J = L \cdot X = \frac{X}{R} \tag{S20}$$

where L is the phenomenological coefficient, which can only be obtained experimentally. In our previous work[4, 5], the reciprocal of the phenomenological coefficient was given a clear physical meaning, i.e., the resistance. Resistance R can be decoupled as shown in **Eq. (S21)**[6]:

$$R = R_{element} \cdot \frac{l}{A} \tag{S21}$$

where, R_{element} is the elementary resistance per transport distance l per transport area A. For an irreversible process, the dissipation function can be written as **Eq. (S22)**:

$$\Psi = \sum JX = \sum \frac{AX^2}{R_{element} l} \tag{S22}$$

Considering the constraint of a certain volume, the final goal is to find the optimal structures leading to minimum dissipation. Thus, an optimization function φ_1 can be established by introducing a Lagrange multiplier λ:

$$\varphi_1 = \sum A \frac{X^2}{R_{element} l} - \lambda \sum Al \tag{S23}$$

Optimizing geometric parameter A, the partial derivative of the optimization function with respect to A should be zero to obtain the minimum dissipation rate. Then, a generalized solution of **Eq. (S23)** can be derived:

$$X = \sqrt{R_{element} \lambda} \cdot l \tag{S24}$$

Substituting **Eq. (S24)** into **Eq. (S20)**, we obtain:

$$J = \frac{A\sqrt{R_{element} \lambda}}{R_{element}} = \sqrt{\lambda / R_{element}}\, A \tag{S25}$$

From mass conservation, the mass flow rates of fluid in parent pipes equal those in children pipes:

$$\frac{A_0^2}{R_{element,0}} = \sum_{i=1}^{N_i} \frac{A_i^2}{R_{element,i}} \tag{S26}$$

Since A_0 and A_i cannot be eliminated, **Eq. (S26)** becomes impractical. Therefore, we introduced optimization of another structural parameter l to derive an effective expression. The optimization function φ_2 is constructed under the constraint of a fixed structural area: $2l_1l_2$=const[7], with another Lagrange multiplier β:

$$\varphi_2 = J_1 \cdot X_1 + J_2 \cdot X_2 - \beta \cdot 2l_1l_2 \tag{S27}$$

Using **Eq. (S24)** and **Eq. (S25)**, **Eq. (S27)** can be rewritten as:

$$\varphi_2 = \lambda A_1 l_1 + \lambda A_2 l_2 - \beta \cdot 2l_1l_2 \tag{S28}$$

Setting the partial derivative of **Eq. (S28)** with respect to l_1 and l_2 to zero yields:

$$l_1 = \frac{\lambda A_2}{2\beta} \tag{S29}$$

$$l_2 = \frac{\lambda A_1}{2\beta} \tag{S30}$$

Combining **Eq. (S26)** with these results gives:

$$\frac{R_{1,element} l_1}{A_1} = \frac{R_{2,element} l_2}{A_2} \tag{S31}$$

According to the definition of mass transport resistance in **Eq. (S21)**, a generalized resistance matching principle can be obtained: optimal transport can be achieved when $R_1 = R_2$.

S5. Models and parameters for quantifying fluid heterogeneity

The fluid density under nanoconfinement has been challenging to measure through in situ experiments [8]. To address this, statistical mechanics methods, such as molecular dynamics (MD) simulations and density functional theory (DFT), have been widely employed to characterize fluid behavior under such conditions. In this study, a hybrid approach combining perturbed-chain statistical associating fluid theory with classical density functional theory (PC-SAFT-DFT) was utilized to analyze fluid heterogeneity in nanoconfined environments.

Within the PC-SAFT framework, fluid density profiles in confined spaces are derived using molecular thermodynamic principles. This model incorporates molecular parameters that quantify fluid-fluid, surface-surface, and fluid-surface interactions, enabling the prediction of fluid states and physical properties influenced by solid surfaces. The accuracy of these predictions has been validated against MD simulation results[9]. As illustrated in **Fig. S1**, key parameters for fluid molecules include m_{seg}, representing the chain length of hard-chain molecules to account for covalent bond effects, σ_{ll} and $\varepsilon_{\mathrm{ll}}$, which denote the size of the repulsive cores and attractive interactions for the segment in the hard chain of the molecules, respectively. The relevant PC-SAFT parameters for the fluids used in this study are provided in **Table S1**.

For solid surface molecules, ρ_{s} denotes the solid atom density, Δ_{s} represents the separation between adjacent surface layers, $\varepsilon_{\mathrm{ss}}$ and σ_{ss} correspond to the energy and size parameters, respectively (**Table S2**). The fluid-surface interactions are described by σ_{ls} and $\varepsilon_{\mathrm{ls}}$ (**Table S3** and **S4**), which represent the size and energy parameters between the surface and fluid, derived by Lorentz-Berthelot mixing rule:

$$\sigma_{ls} = \frac{\sigma_{ll} + \sigma_{ss}}{2} \tag{S32}$$

$$\varepsilon_{ls} = \sqrt{\varepsilon_{ll}\varepsilon_{ss}} \tag{S33}$$

In PC-SAFT-DFT, the density profiles $\rho(z)$, as shown in **Fig. S1,** are acquired by minimizing the grand potential (Ω) of the Euler–Lagrange equation:

$$\frac{\delta\Omega\left[\rho(z)\right]}{\delta\rho(z)} = \frac{\delta A\left[\rho(z)\right]}{\delta\rho(z)} - \left(\mu_b - mV_{ext}(z)\right) = 0 \tag{S34}$$

Following the PC-SAFT equation of state, the Helmholtz free energy A can be described as [10]:

$$V_{ext}\left(z\right)=u_{ls}\left(z\right)+u_{ls}\left(d-z\right) \tag{S35}$$

where A^{id} is the ideal free energy, A^{hs}, A^{chain}, A^{disp}, and A^{assoc} are the excess free energies due to hard sphere, chain, dispersive, and associative interactions, respectively. In addition, according to DFT, $V_{ext}(z)$ represented the external field acting on the segments, which can be obtained by the surface-fluid interaction at the position of solvent molecules[11].

$$V_{ext}\left(z\right)=u_{ls}\left(z\right)+u_{ls}\left(d-z\right) \tag{S36}$$

For the fluid molecules in nano channels, the Steele 10-4-3 potential, together with the PC-SAFT parameters, was used to describe the surface-fluid interactions [10]:

$$u_{ls}\left(z\right)=2\pi\rho_s\Delta_s\varepsilon_{ls}\sigma_{ls}^2\left[\frac{2}{5}\left(\frac{\sigma_{ls}}{z}\right)^{10}-\left(\frac{\sigma_{ls}}{z}\right)^{4}-\left(\frac{\sigma_{ls}^4}{3\Delta_s\left(z+0.61\Delta_s\right)^3}\right)\right] \tag{S37}$$

The minimum of Ω in **Eq. (S34)** is determined by chemical potential equilibrium between the confined fluid with the density profile ρ(z) (**Fig. S1)** and the bulk fluid under bulk pressure and temperature. Picard iteration is employed to solve the density profile[12]. To bridge microscopic fluid distribution and macroscopic mass transport behaviors under nanoconfinement, the average confined fluid density ρ_{avg} was used:

$$\rho_{avg}=\frac{1}{2r}\int_{-r}^{r}\rho\left(z\right)dz \tag{S38}$$

While viscosity and density are strongly correlated, quantifying confined fluid viscosity remains challenging due to its dynamic nature. Our previous work established a correlation model between confined density and viscosity via the self-diffusion coefficient D_e[13]. Specifically, D_e relates to ρ_{avg} through **Eq. (S39)**[14]:

$$\begin{aligned}D_e=&\frac{3}{8\rho^* m_{seg}^{1/6}}\sqrt{\frac{k_BT^*}{\pi m}}\left(1-\frac{\rho^*}{a\left(T^*\right)^b}\right)\left[1+\left(\rho^*\right)^c\left(\frac{P_1\left(\rho^*-1\right)}{P_2\left(\rho^*-1\right)+\left(T^*\right)^{\left(P_3+P_4\rho^*\right)}}+P_5\right)\right]\\&\times\exp\left(-\frac{\rho^*}{2T^*}\right)\times\exp\left\{S_1\left(m_{seg}-1\right)+S_2\left(m_{seg}-1\right)^{3/2}\rho^*\left(T^*\right)^{1/2}\right.\\&\left.+S_3\left(m_{seg}-1\right)\rho^*\left[1+\left(\frac{T^*}{0.527}\right)^{1/2}\right]^{-1/2}\right\}\end{aligned} \tag{S39}$$

This equation for chain-like fluids incorporates density, temperature, and PC-SAFT parameters, and has been proven to be suitable for gas, liquid, and supercritical states[15]. Here, $\rho^* = \rho_{avg} m_{seg} \sigma_{ll}^3 N_A / M$, $T^* = k_B T / \varepsilon_{ll}$, N_A is the Avogadro constant, M is the molecular weight, k_B is the Boltzmann constant, and m is the molecular mass. The parameters a, P_1, P_2, P_3, P_4, P_5, S_1, S_2, and S_3 are listed in **Table S5**.

Confined viscosity η_{avg} was then derived from D_e using the Stokes-Einstein equation[16]:

$$\eta_{avg} = \frac{k_B T}{3\pi D_e \sigma_{ll}} \tag{S40}$$

Using these physical property models of nanoconfinement fluids, we studied how fluid-liquid interactions affect ρ_{avg} and η_{avg}. **Fig. S2** to **S4** show distinct deviations of ρ_{avg} and η_{avg} from bulk properties (ρ_{bulk} and η_{bulk}) across pore sizes. Specifically, in macropores ($d \geq 50$ nm), fluid properties match bulk values. In mesopores (d = 2~50 nm), deviations increase with decreasing d, as a higher proportion of molecules suffered by surface interactions. Most importantly, owing to the molecule packing effects, ρ_{avg} oscillates with micro pore size (when $d < 2$ nm), consistent with MD simulations[17].

These oscillations induce corresponding viscosity fluctuations. For the ranges of oscillation, two critical observations emerge: (1) Density reductions of 14.1~98.6% in 0.5~2 nm cause viscosity to approach gas-phase values, drastically altering transport mechanisms; (2) Sharp property variations with minor pore size changes highlight the precision required for microporous structure design.

Comparisons between nonpolar and polar fluids on nonpolar (graphene) and polar (Ti_3C_2 and graphene-Ti_3C_2) surfaces reveal: (1) for nonpolar fluids, fluid heterogeneity is less affected by different surfaces, and the molecule size effects plays a dominant role (**Fig. S2**); (2) for polar fluids, ρ_{avg} and η_{avg} in microporous graphene showed an unlike form compared to Ti_3C_2 and graphene-Ti_3C_2 (**Fig. S3** and **S4**), which is due to the different interaction mechanisms with nonpolar and polar surface (see energy parameters in **Table S1**).

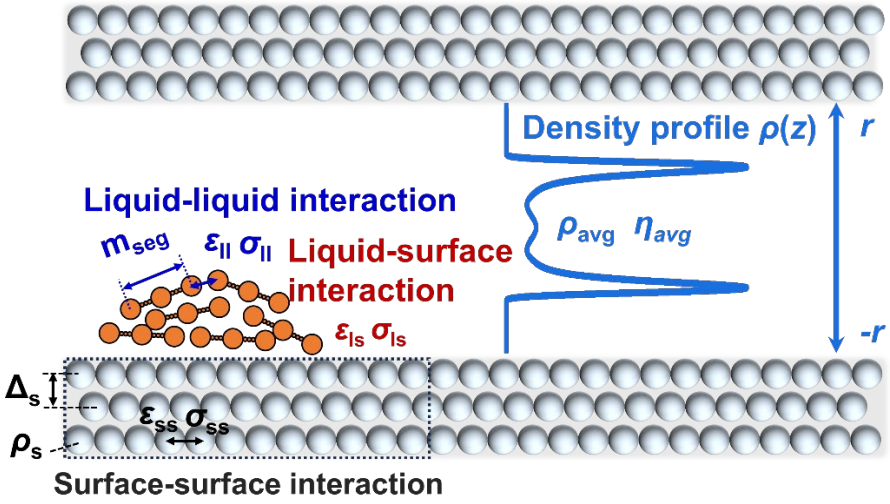

Fig. S1. Schematic diagram of molecular interaction for the fluid within nanopore channels

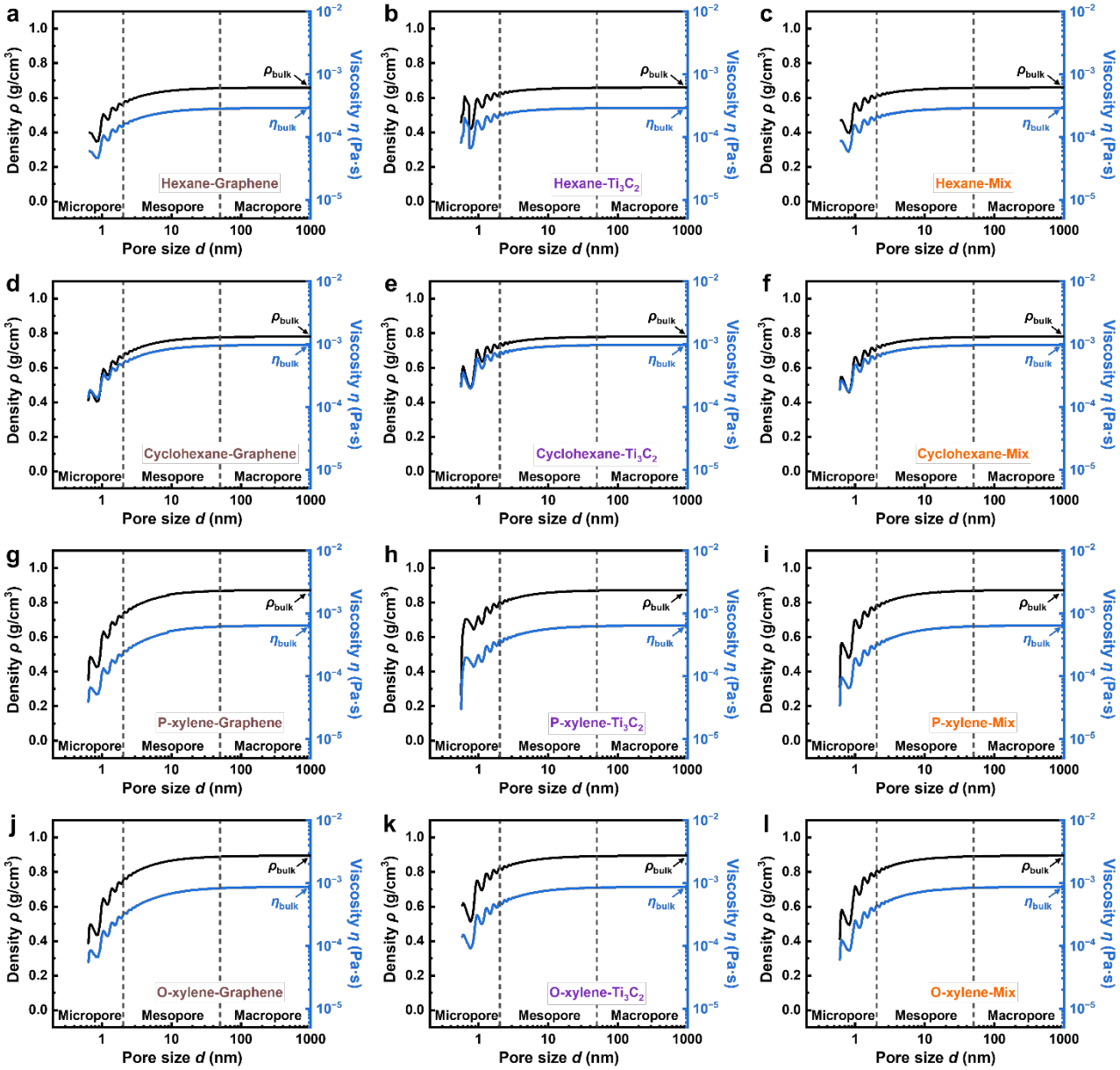

Fig S2. The average density and viscosity of nonpolar fluid (hexane, cyclohexane, *p*-xylene, and *o*-xylene) in 0.5~1000 nm nanopores of graphene, Ti_3C_2, and graphene-Ti_3C_2 (Mix)

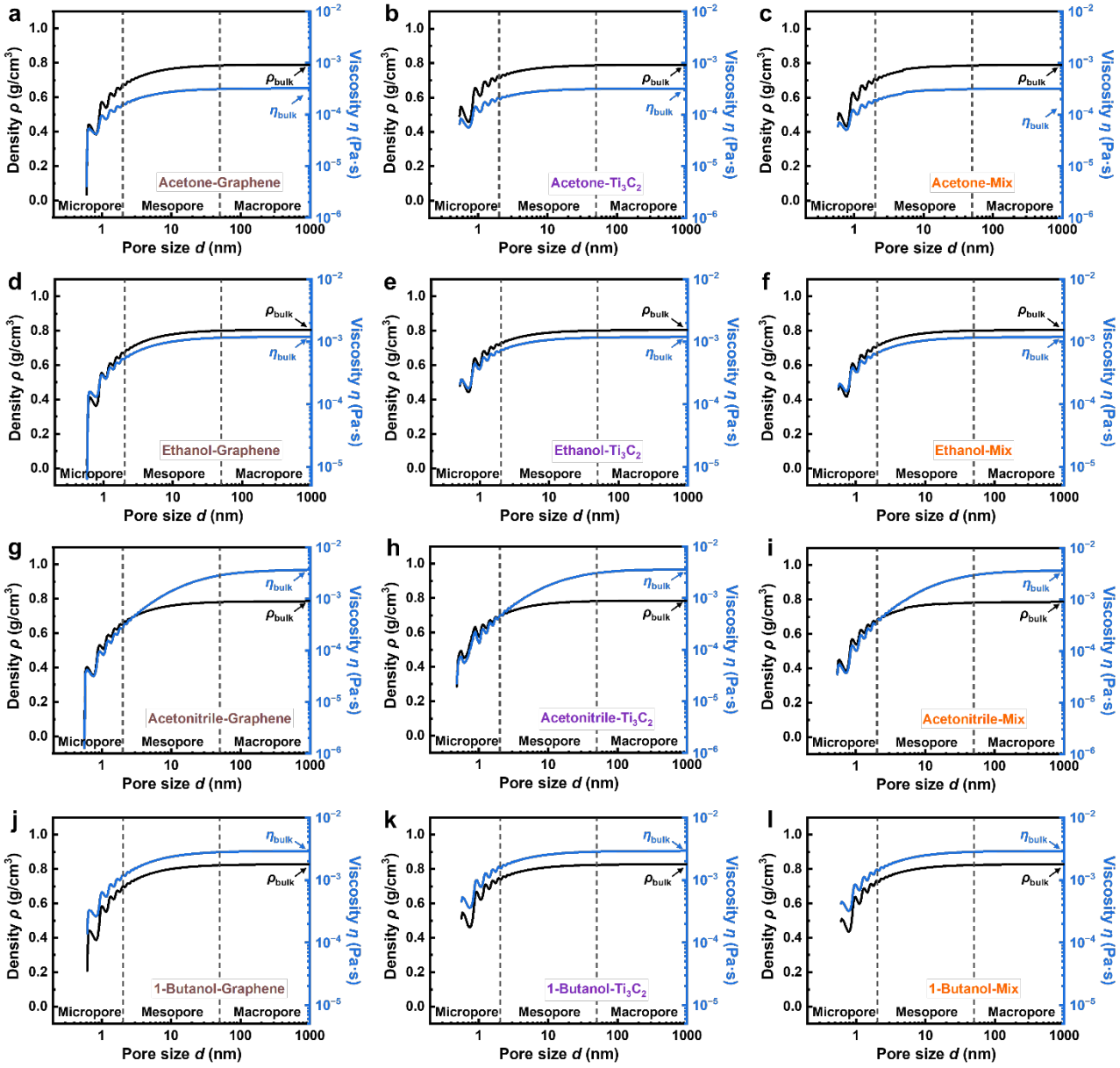

Fig S3. The average density and viscosity of weakly polar fluid (acetone, ethanol, acetonitrile, and 1-butanol) in 0.5~1000 nm nanopores of graphene, Ti_3C_2, and graphene-Ti_3C_2 (Mix)

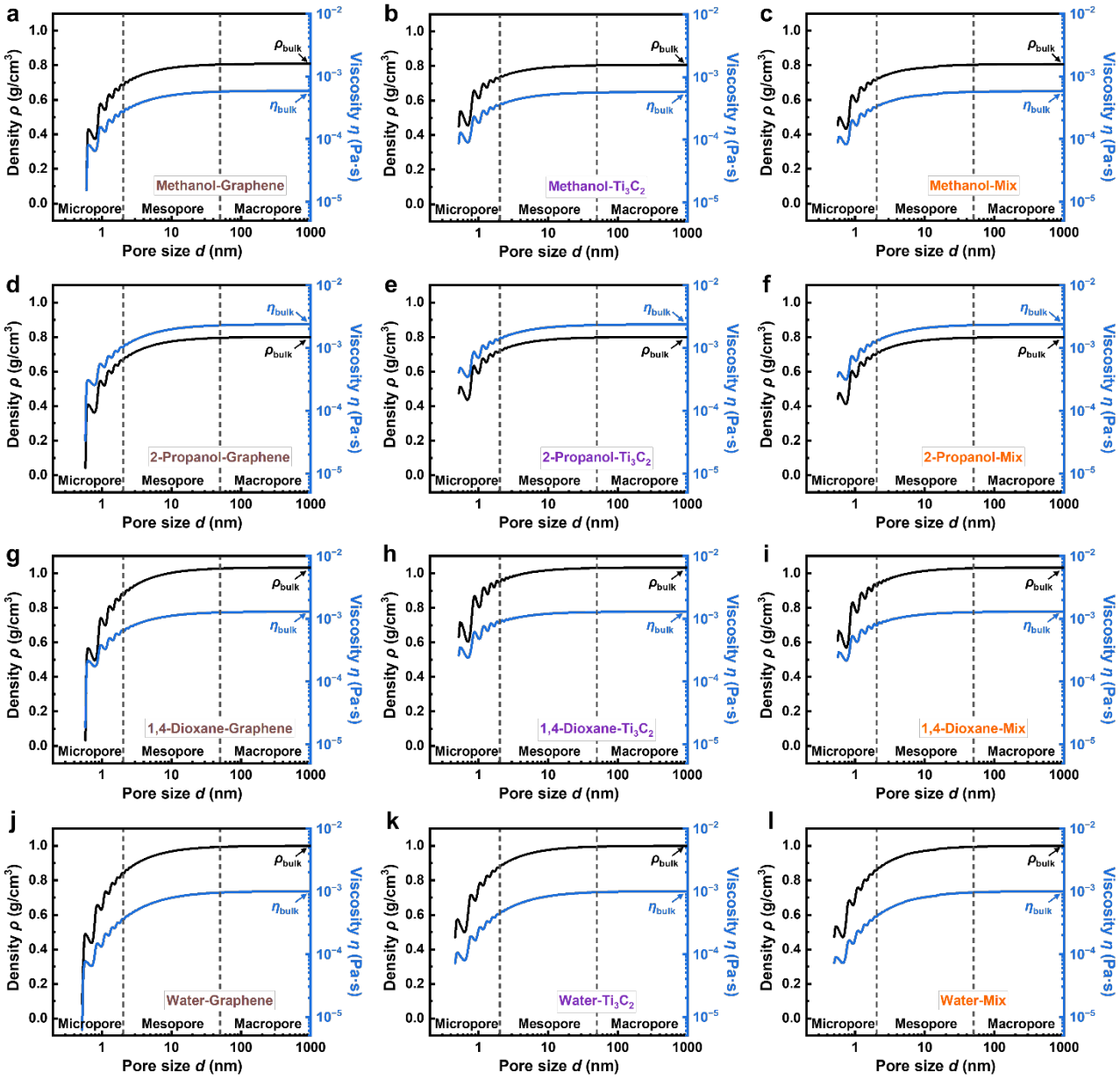

Fig S4. The average density and viscosity of highly polar fluid (methanol, 2-propanol, 1,4-dioxane, and water) in 0.5~1000 nm nanopores of graphene, Ti_3C_2, and graphene-Ti_3C_2 (Mix)

Table S1. Molecular parameters of fluids. PC-SAFT parameters for the fluid molecules [6, 12].

Fluid Type	Fluid	m_{seg}	$\varepsilon_{seg}^{tot}/k_B$ (K)	$\varepsilon_{seg}^{disp}/k_B$ (K)	σ_{seg} (Å)
nonpolar	Hexane	3.51	262.32	262.32	3.67
	Cyclohexane	2.53	278.11	278.11	3.85
	P-xylene	3.17	283.77	283.77	3.78
	O-xylene	3.14	291.05	291.05	3.76
weakly polar	Acetone	2.22	312.26	259.99	3.61
	Ethanol	2.38	305.41	198.24	3.18
	Acetonitrile	2.26	648.56	311.31	3.35
	1-Butanol	2.75	312.72	259.59	3.61
highly polar	Methanol	1.53	396.45	188.90	3.23
	2-Propanol	3.09	259.72	208.42	3.21
	1,4-Dioxane	2.90	284.15	279.60	3.40
	Water	1.20	334.20	77.9	2.80
/	Hydrogen	0.83	29.2	29.2	2.87
	Oxygen	1.77	114.9	115.0	3.21
	Hydrogen peroxide	2.02	298.3	204.0	3.80

For the size parameters of the fluid in **Eq. (S32)**, $\sigma_{ll} = \sigma_{seg}$ represents the fluid-fluid size parameter of the segment in hard-chain fluid molecules. But for the energy parameters of fluid in **Eq. (S33)**, the PC-SAFT energy parameters differ depending on fluid polarity, thus, their selection must be carefully justified. Specifically, (1) for nonpolar fluids, the total energy parameter equals the dispersion energy ($\varepsilon_{ll} = \varepsilon_{seg}^{tot} = \varepsilon_{seg}^{disp}$); (2) for polar fluids, $\varepsilon_{seg}^{tot} \neq \varepsilon_{seg}^{disp}$, energy parameters are determined by surface's polarity:

1. for polar surfaces (Ti_3C_2 and Graphene-Ti_3C_2), the total energy parameter including both dispersion and association contributions are used to calculate the fluid-surface interactions ($\varepsilon_{ll} = \varepsilon_{seg}^{tot}$)[18].

2. for nonpolar surfaces (Graphene and carbon), dispersion-free energy dominates the fluid-surface interactions ($\varepsilon_{ll} = \varepsilon_{seg}^{disp}$).

Table S2. Molecular parameters of solid surface. Steele 10-4-3 potential parameters of Graphene, Ti_3C_2, Graphene-Ti_3C_2, Silica, BioMC, and Cabot [6, 12].

	ρ_s (Å^{-3})	Δ_s (Å)	σ_{ss} (Å)	ε_{ss}/k_B (K)
Graphene	0.114	3.35	3.40	28.0
Ti_3C_2	0.055	9.93	2.54	78.2
Graphene-Ti_3C_2	0.085	6.64	2.97	53.1
Silica	0.044	2.20	2.70	230
BioMC	0.067	1.52	3.21	36.09
Cabot	0.061	1.52	3.11	31.19

Table S3. Intermolecular parameters in membrane system. Size and Energy parameters between twelve types of fluids and three membrane surfaces (Graphene, Ti_3C_2, and Graphene-Ti_3C_2).

Fluids	Graphene		Ti_3C_2		Graphene-Ti_3C_2	
	σ_{ls} (Å)	ε_{ls}/k_B (K)	σ_{ls} (Å)	ε_{ls}/k_B (K)	σ_{ls} (Å)	ε_{ls}/k_B (K)
Hexane	3.54	85.70	3.11	143.23	3.32	118.02
P-xylene	3.59	89.14	3.16	148.97	3.38	122.75
O-xylene	3.58	90.27	3.15	150.86	3.37	124.32
Cyclohexane	3.63	88.24	3.20	147.47	3.41	121.52
Acetone	3.51	85.32	3.08	156.26	3.29	128.77
Ethanol	3.29	74.50	2.86	154.54	3.08	127.35
Acetonitrile	3.38	93.36	2.95	225.21	3.16	185.58
1-Butanol	3.51	85.26	3.08	156.38	3.29	128.86
Methanol	3.32	72.73	2.89	176.07	3.10	145.09
2-Propanol	3.31	76.39	2.88	142.51	3.09	117.44
1,4-Dioxane	3.40	88.48	2.97	149.07	3.19	122.83
Water	3.10	46.70	2.67	161..66	2.89	133.21

Table S4. Intermolecular parameters in heterogeneous catalysis system. Size and Energy parameters between four fluids and two carbon surfaces (BioMC and Carbon).

Fluids	BioMC		Cabot	
	σ_{ls} (Å)	ε_{ls}/k_B (K)	σ_{ls} (Å)	ε_{ls}/k_B (K)
Hydrogen	3.04	32.46	2.99	30.18
Oxygen	3.21	64.42	3.16	59.89
Hydrogen peroxide	3.51	85.80	3.46	79.77
Water	3.01	53.03	2.96	48.50

Table S5. The generalized parameters in self-diffusion coefficient equation as shown in Eq. (S39).

Generalized parameters	Value
a	1.029079
P_1	0.596103
P_2	0.539292
P_3	0.400152
P_4	-0.41054
P_5	0.68856
S_1	0.21900
S_2	0.19900
S_3	-1.80000

S6. Models and parameters for quantifying slip length

In fluid mechanics, slip length b is a key parameter in the Navier-Stokes slip boundary condition, describing interfacial effects on flow. However, accurately predicting b remains challenging. To relate b to interfacial properties, liquid–solid friction analysis provides a framework, Bocquet et al[19] derived a microscopic expression for b via the Green-Kubo relation and density–density correlation function:

$$b = \frac{2Dq_{\|}k_B T\eta}{S\left(q_{\|}\right)\int dz\left\langle\rho\left(z\right)\right\rangle V_{ext}\left(z\right)^2} \tag{S41}$$

where $Dq_{\|}$ is the collective diffusion coefficient, $S\left(q_{\|}\right)$ is the two-dimensional structure factor, and $\int dz\left\langle\rho\left(z\right)\right\rangle V_{ext}\left(z\right)^2$ is the total force on fluid molecules. Notably, **Eq. (S41)** assumes bulk fluid properties, failing for nanoconfined fluids (especially in micropores with oscillatory properties, **Fig S2** to **S4**)**.** Therefore, we modified **Eq. (S41)** into **Eq. (S42)** for nanoconfined systems in previous work[12]:

$$b = \frac{2\left(k_B T\right)^2}{3\pi\sigma_{ll}\rho_{fir}\int_{\sigma_{ll}+\delta}^{+\infty} dz V_{ext}\left(z\right)^2} \tag{S42}$$

where ρ_{fir} is the average density in the range of the first fluid layer, and σ_{ll} is the molecular size. From nanoconfined density profiles (**Fig S5**), the first fluid layer dominates slip phenomena, as slip primarily occurs at the fluid-solid interface[20]. Here, ($\sigma_{\mathrm{ll}} + \delta$) represents the first layer span, including the density peak (σ_{ll}) and rarefied gas region (δ). Similar first-layer profiles across pore sizes arise from competing fluid-fluid and fluid-surface interactions. We thus proposed a semi-empirical b model using the Steele 10-4-3 potential and PC-SAFT parameters[12]:

$$b = A_i\left(m_{seg}\rho_s\Delta_s\sigma_{ls}^2\varepsilon_{ls} - B_i\right)^2 + C_i \tag{S43}$$

With the model parameters A_{i}, B_{i}, and C_{i} listed in **Table S6**. Using molecular parameters (**Table S1** to **S4**), calculated b values are given in **Table S7** and **S8**. Furthermore, considering the application of this model in practical conditions, for real surfaces with non-ideal roughness and surface properties, we linked **Eq. (S43)** to experimentally measurable contact angle θ_{c}:

$$b_{real} = \frac{k}{\alpha_{w,real}^2} = \frac{k}{\left[0.6\ln\left(180^\circ/\theta_c\right)\right]^2} \tag{S44}$$

wherein, a correlation between b and θ_c via wetting parameter α_w (proposed by Gubbins et al[18] to connect the intermolecular interactions with macroscopic wetting property, α_w of fluid on ideal surface was defined as $\alpha_{w,ideal} = \rho_s \Delta_s \sigma_{ls}^2 \varepsilon_{ls} / \varepsilon_{ll}$), i.e., $\theta_c = 180° \exp(-\alpha_{w,real}/0.6)$ was used, which was established by Zhao et al[17]. Solvophobic surfaces ($\theta_c > 90°$) exhibit lowα_w and large b, reflecting reduced friction. Conversely, solvophilic surfaces presented large α_w and low b.

The fluid-specific parameter k in **Eq. (S44)** (k = 1.28 nm for benzene[17]) limits generalizability. By combining **Eq. (S43)** and **Eq. (S44)**, k can be determined from ideal b and α_w, yielding **Eq. (S45)**:

$$b_{real} = \frac{\left[A_i \left(m_{seg} \rho_s \Delta_s \sigma_{ls}^2 \varepsilon_{ls} - B_i \right)^2 + C_i \right] \cdot \left[\rho_s \Delta_s \sigma_{ls}^2 \varepsilon_{ls} / \varepsilon_{ll} \right]^2}{\left[0.6 \ln \left(180^\circ / \theta_c \right) \right]^2} \tag{S45}$$

This model quantifies surface modification effects using experimental θ_c. We use it to estimate b of water-graphene in practical systems, listing in **Table S9**. Slip length of water on graphene can range from about 4~150 nm by regulating the surface roughness and surface properties of graphene, aligning with the results of simulations and experiments[21, 22, 23]. In other words, these advances in modelling b can successfully explain the super-fast water transport phenomena in graphitic nanochannels[24, 25, 26, 27], and bridges the gap between microscopic interactions and macroscopic transport behavior, providing a solid foundation for the rational design of Murray nanomaterials' optimal hierarchical structures.

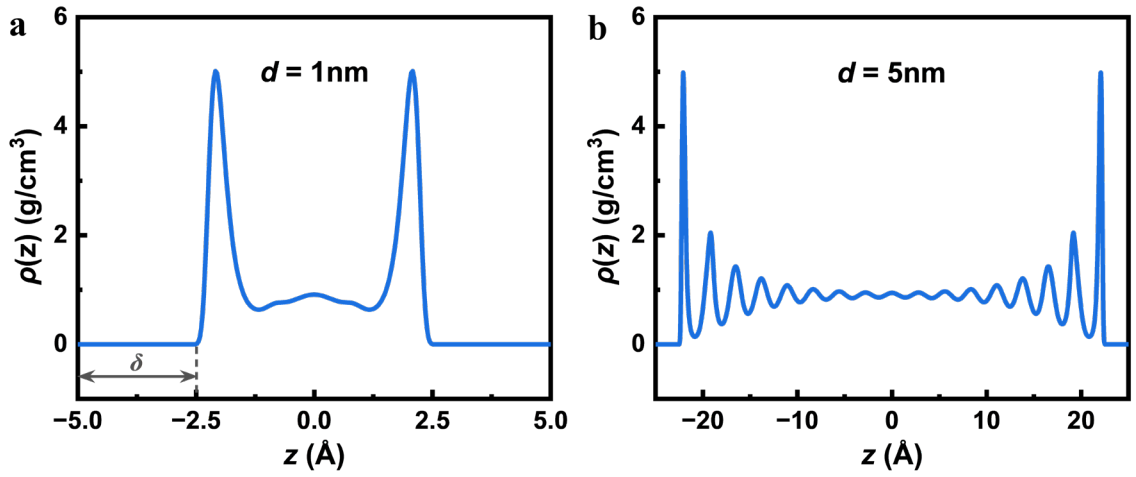

Fig S5 Density profiles of fluid molecules in nanopores. Water in Graphene pore channels with different pore size was taken as the example: (a) pore size d = 1 nm; (b) d = 5 nm

Table S6. The parameters in slip length model shown in Eq. (S43).

Model parameters	Value
A_1/nm	2.54049×10^{-6}
B_1/K	137.8464
C_1/nm	0.200134
A_2/nm	2.93049×10^{-6}
B_2/K	1994.547
C_2/nm	0.416563

According to the strength of fluid-surface and fluid-fluid interactions, different model parameters should be selected for the slip length model shown in **Eq. (S43)**. More specifically, for systems with weak fluid-surface interactions (when $m_{seg}\rho_s\Delta_s\sigma_{ls}^2\varepsilon_{ls}/\varepsilon_{ll}\le3.8$), the first set of model parameters are used (i = 1), and for systems with strong fluid-surface interactions (when $m_{seg}\rho_s\Delta_s\sigma_{ls}^2\varepsilon_{ls}/\varepsilon_{ll}>3.8$), another set of parameters (i = 2) are valid. As evaluated[12], the slip length calculation error can be controlled within 5.4%, which is acceptable for the nanoscale fluid flow studies[28].

Table S7. Slip length of fluid flow on solid surface calculated by Eq. (S43). For twelve kinds of fluids in membrane separation system.

Fluids	Slip length (Å)		
	Graphene	**Ti_3C_2**	**Graphene-Ti_3C_2**
Hexane	13.32	17.41	13.81
Cyclohexane	26.55	4.47	10.85
P-xylene	14.84	14.73	11.46
O-xylene	15.03	14.32	11.16
Acetone	40.01	5.22	6.06
Acetonitrile	38.14	7.00	27.04
Ethanol	11.00	7.53	8.45
1-Butanol	4.91	5.95	4.98
Methanol	4.73	32.31	30.47
2-Propanol	6.26	4.16	4.22
1,4-Dioxane	28.11	4.70	12.67
Water	97.94	48.76	49.67

Table S8. Slip length of fluid flow on solid surface calculated by Eq. (S43). For four kinds of fluids in the carbon-based catalyst system

Fluids	Slip length (Å)	
	BioMC	**Cabot**
Hydrogen	2.32	2.35
Oxygen	2.01	2.04
Hydrogen peroxide	2.09	2.04
Water	2.36	2.21

Table S9. The contact angle θ_c, wetting parameter α_w, slip length b of water in graphene nanochannels with different surface modifications.

Surfaces	θ_c (°)	α_w (/)	b (Å)
Hydrophobic graphene [29]	152	0.11	1495.87
Graphene (model) [12]	88	0.43	97.94
Hydrophilic graphene [30]	5	2.15	39.16

For graphene in the model system as mentioned above, slip length in **Table S7** is used to estimate the ideal contact angle and wetting parameter of water on solid surface. Then, α_w and b of water on hydrophobic and hydrophilic graphene are calculated by θ_c based on **Eq. (S45)**.

S7. The role of interfacial slip and fluid heterogeneity on Murray's law

As shown in **Eq. (S21)**, the elementary mass transport resistance R_{element} per mass transport distance l per mass transport area A is employed to describe the mass transport capacity of pore channels. Combining the slip-modified HP equation as **Eq. (S1)**, R_{element} can be decoupled as viscous resistance R_η and slip resistance R_λ:

$$\frac{1}{R_{element}} = \frac{1}{1/R_\eta + 1/R_\lambda} = \frac{1}{\frac{r^2\rho_{ave}}{8\eta_{ave}} + \frac{r\rho_{ave}b}{2\eta_{ave}}} \tag{S46}$$

where R_λ represents the influence of interfacial effects, incorporating slip length b. Since the total flow rate J_{total} equals the sum of viscous flow rate J_η and slip flow rate J_λ, the total resistance R_{total} (i.e., R_{element}) takes the form of a parallel resistance network as shown in **Eq. (S46)**. The factors γ_η and γ_λ are defined to quantify viscous and slip flow contributions:

$$\gamma_\eta = \frac{J_\eta}{J_{total}} = \frac{R_{element}}{R_\eta} \tag{S47}$$

$$\gamma_\lambda = \frac{J_\lambda}{J_{total}} = \frac{R_{element}}{R_\lambda} \tag{S48}$$

Because parallel resistance is always lower than individual resistances, γ_η and γ_λ are less than one, with $\gamma_\eta + \gamma_\lambda = 1$. We analyzed R_{element}, R_η and R_λ across 36 fluid-surface systems (**Fig S6** to **S8**). The dominated mechanism is defined here as the contribution factor γ of it was larger than 80%, then we can get the range of b = 0.49~1.74 nm for validity of resistance-dominated criterion based on pore sizes as shown in **Fig. 2c**. When b is greater than 1.74, slip-dominated flow even can be extended to 2~20 nm pore channels. In addition, the slip flow can only be ignored in macropores when b < 0.49 nm, which is indispensable in meso- and micro-pores.

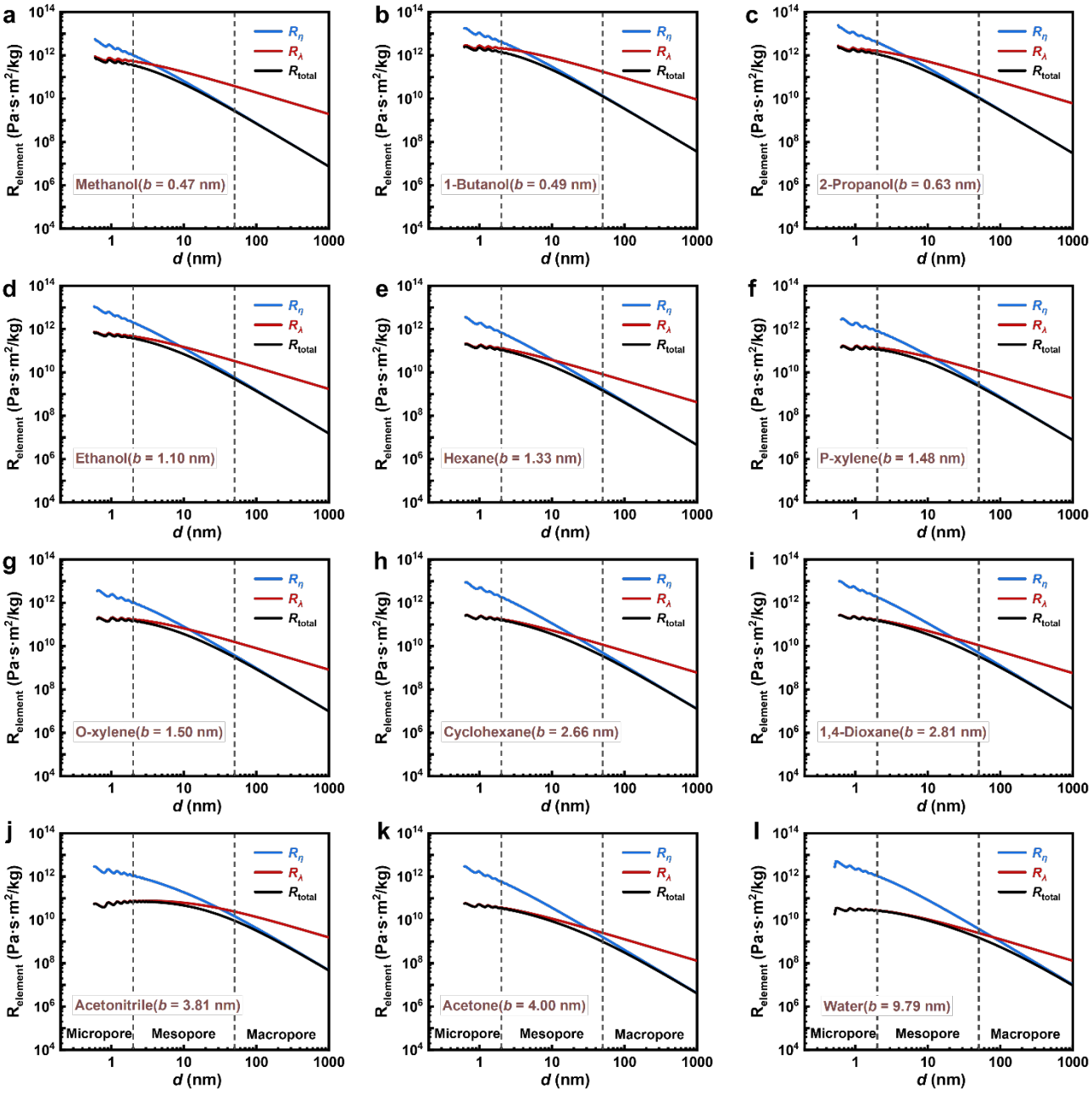

Fig S6. The flow resistance of different fluids in graphene channels with 0.5~100 nm diameters.
a-l figures were sorted by the slip length of fluid-surface from small to large.

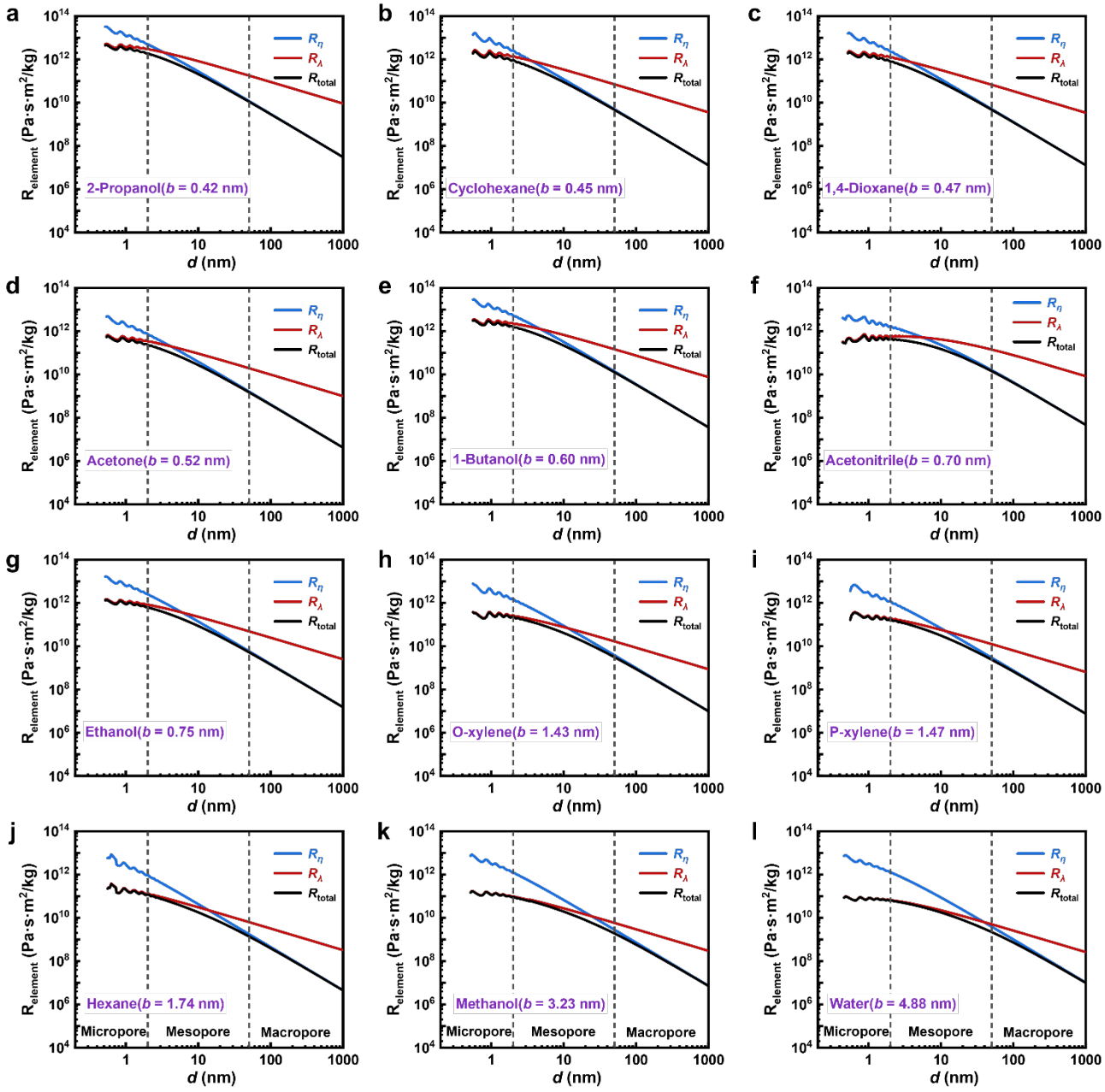

Fig S7. The flow resistance of different fluids in Ti_3C_2 channels with 0.5~100 nm diameters. *a-l* figures were sorted by the slip length of fluid-surface from small to large.

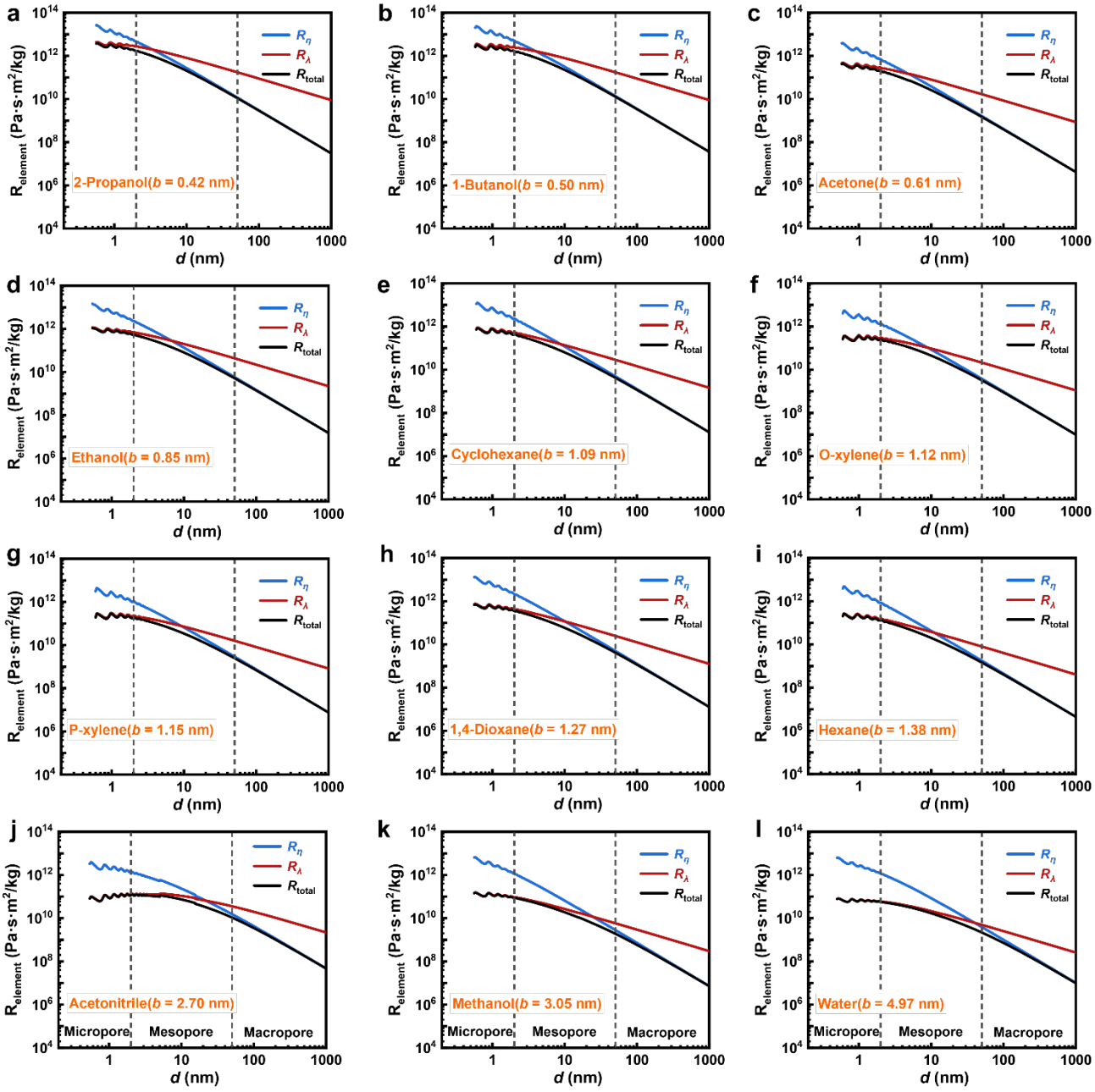

Fig S8. The flow resistance of different fluids in graphene-Ti_3C_2 channels with 0.5~100 nm diameters. *a-l* figures were sorted by the slip length of fluid-surface from small to large.

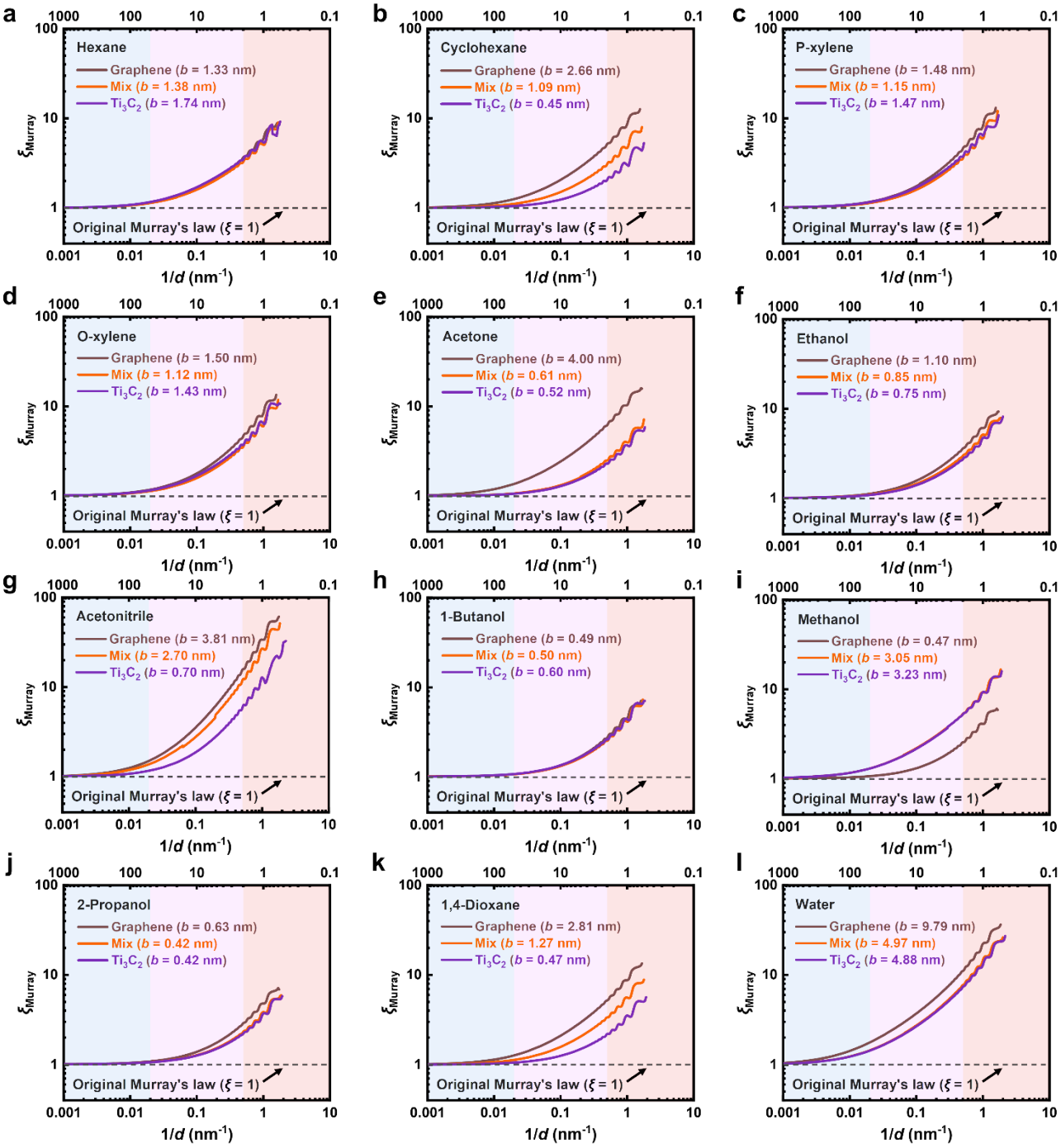

Fig S9. The modifying factor ξ_{Murray} of Murray's law for different fluids flow in hierarchical nanomaterials with 10 μm parent pipes as shown in Fig. 2d.

S8. Hydrodynamic experiments by atomic force microscopy (AFM)

S8.1 Materials

Silica colloidal probes for AFM were prepared according to Ducker et al[31]. Monodisperse silica microspheres (purchased from Zhongke Leiming Technology Co., Ltd, Beijing) aqueous suspension were deposited onto glass substrate or freshly cleaved mica surface. After solvent evaporation, the cantilever (nominal spring constant: 0.35 N/m) was mounted onto the atomic force microscope's scanning head with laser alignment. A small amount of epoxy glue (from UHU, Germany) was then applied to the cantilever tip (NP-O10-A, from Bruker, USA). The cantilever was subsequently brought into controlled contact with the silica microsphere, maintaining this contact for 20 s to achieve preliminary adhesive bonding. Lastly, the colloidal probe assembly was elevated and transferred to a contamination-free environmental chamber for final curing (>24 h at ambient conditions).

Flat substrates comprised self-made, surface-modified silica wafers. Surface functionalization protocols: (1) Hydrophilic treatment: Si (100) wafers with 100 nm thermal oxide layer (silica) were immersed in hot piranha solution (1:3 v/v H_2O_2/H_2SO_4) for 30 min under ambient ventilation conditions[32]. (2) Hydrophobic treatment: Parallel samples were etched in hydrofluoric acid (HF) for 30 min. All substrates were rinsed with ultrapure water and ethanol, then dried under N_2.

Perhydrol (H_2O_2, 30 wt%), sulfuric acid (H_2SO_4, 98 wt%) and hydrofluoric acid (HF, 40 wt%) were sourced from Shanghai Lingfeng Chemical Reagent Co., Ltd. The anhydrous ethanol (C_2H_5OH) was purchased from Sigma-Aldrich (anhydrous, ≥ 99.5%), and the high-quality ultrapure water was used in all the related systems by Ultrapure water machine from EPED.

S8.2 Characterization

Probe morphology and microsphere diameter were characterized under vacuum by field emission scanning electron microscopy (FESEM, Hitachi S-4800). Wettability was measured via sessile drop metho (TX500C surface tensiometer, Zhongchen digital technology equipment Co, China) at 20 ℃. Contact angles of the water on silica wafers (untreated, hydrophilic and hydrophobic treated) are shown in **Fig. S10**.

S8.3 Hydrodynamic force measurement

Colloidal probe AFM (Bruker Dimension ICON, USA) experiments were conducted at 20 ± 1 °C. The colloidal probe was mounted on a holder, and the substrate was secured in the fluid cell. Contact mode operation was initiated following laser alignment optimization over the cantilever.

Surface topography was preliminarily characterized through 10×10 μm^2 scans in contact mode, where regions with root-mean-square roughness below 1 nm were selected for hydrodynamic measurements. The hydrodynamic experiments were performed by the colloidal probe approaching the modified silica surfaces in water environment, and the hydrodynamic force F_d profiles were acquired when the colloidal probe was pressed down in the z-axis direction to reach the surface with a controlled approach velocities v_z = 24.42 μm/s. Taking the average of multiple measurements, the initial distance z_0 between colloidal probe and the silica substrate was obtained based on the displacement required for their contact. In addition, actual displacement $\Delta z'$ of colloidal probe should be corrected by the deflection δ of the probe, i.e., $\Delta z' = \Delta z - \delta$, where Δz was the displacement given by instrument. Separation $d = z_0 - \Delta z'$, and approach rates v_z were derived from $d(t)$ differentiation.

S8.4 Model analysis

The colloidal probe diameter was d_0 = 45.7 μm (**Fig. S11**). Measurable quantities included F_d, v_z, and the separation d_1 between the sphere and the surface (**Fig. S12a**). Data with $d_1 \leq 50$ nm were analyzed to ensure laminar flow. Water motion beneath the probe involved axial displacement and radial drainage (**Fig. S12b**).

Within a certain period of time t, the probe decreased dz, and the corresponding volumetric flow dQ can be used to describe the flux J of this process:

$$J = \frac{dQ}{dt} = \frac{\pi d_0^2}{4} \cdot \frac{dz}{dt} = \frac{\pi d_0^2 v_z}{4} \tag{S49}$$

Driving force ΔP was calculated from load F_d and load area A_0:

$$\Delta P = \frac{F_d}{A_0} - P_0 = \frac{F_d}{\pi d_0^2 / 4} - P_0 \approx \frac{4F_d}{\pi d_0^2} \tag{S50}$$

where the pressure difference can be simplified as hydraulic pressure, due to the hydraulic pressure caused by the load being much greater than the ambient pressure P_0. Then, the total mass transport resistance R_{exp} based on experimentally measured F_d can be expressed as:

$$R_{\exp} = \frac{\Delta P}{J} = \frac{16F_d}{\pi^2 d_0^4 v_z} \tag{S51}$$

However, Reynolds lubrication theory has given the theoretical expression of F_d:

$$F_d = \frac{3\pi\eta d_0^2 v_z}{2d_1} \tag{S52}$$

where the viscous resistance of fluid in bulk R_{bulk} was considered as the sole hindrance for fluid flow. Therefore, substituting **Eq. (S52)** into **Eq. (S51)**, the expression of R_{bulk} can be written as:

$$R_{bulk} = \frac{24\eta_{bulk}}{\pi d_0^2 d_1} \tag{S53}$$

Where R_{bulk} assumes no-slip boundaries and bulk viscosity. Therefore, deviations between R_{exp} with R_{bulk} reflect nanoscale effects of fluid heterogeneity and interfacial slip.

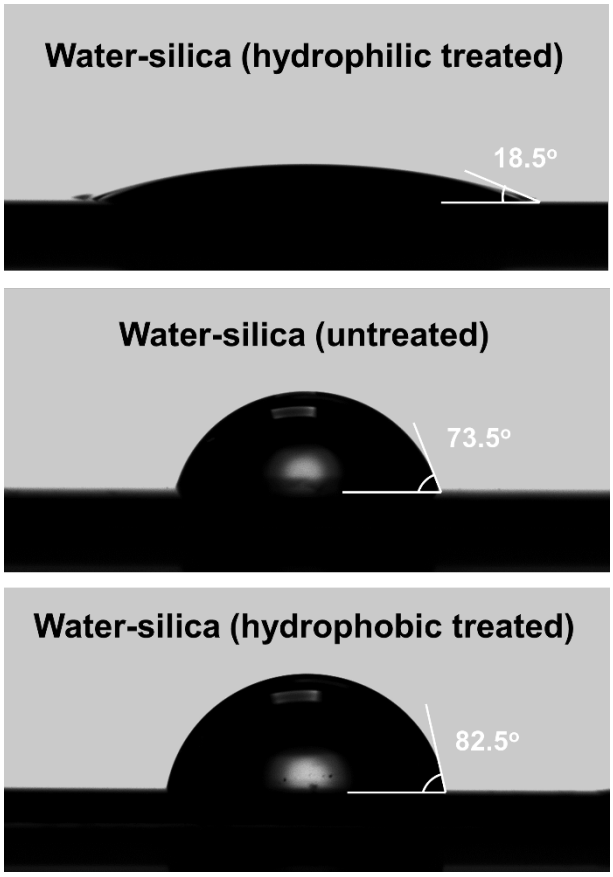

Fig. S10. Wettability of the flat substrates used in AFM hydrodynamic experiments. Contact angle measurements of water on the silica (untreated, hydrophilic, and hydrophobic treated)

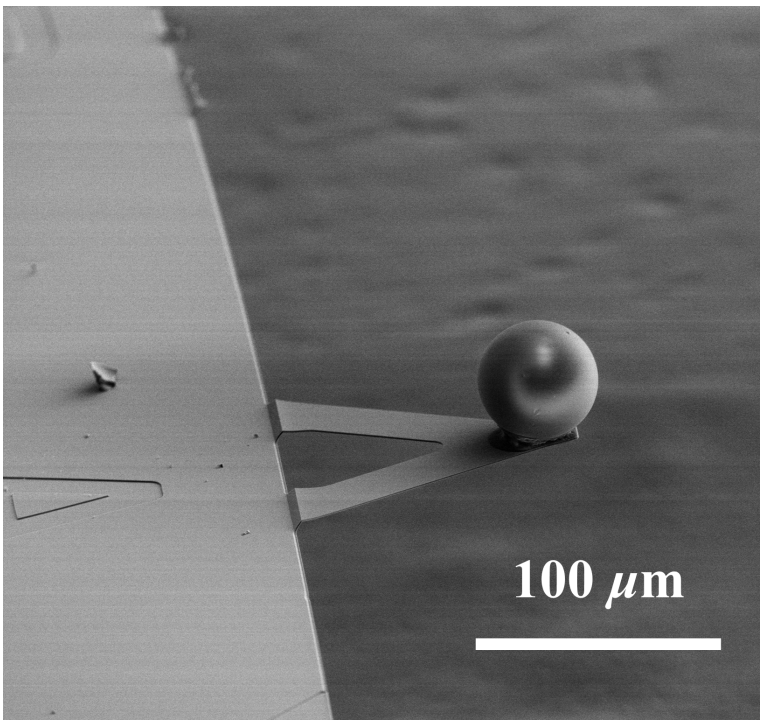

Fig. S11. Scanning electron microscopy image of AFM colloidal probe. The spherical diameter of the probe was about 45.7 μm.

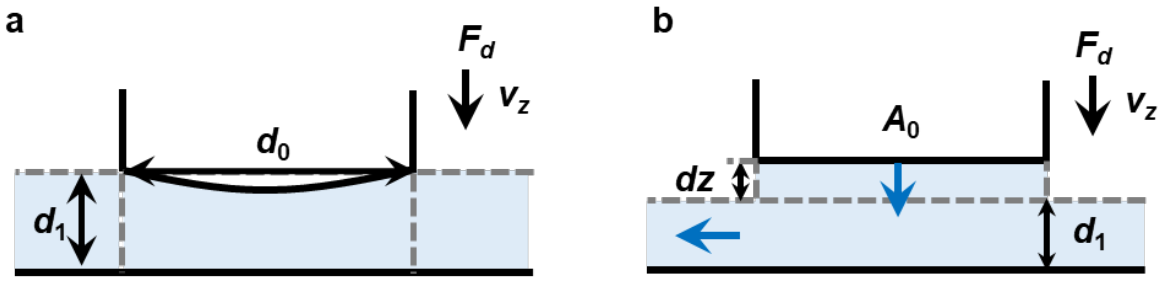

Fig. S12. Schematic diagrams of AFM hydrodynamics experiments. a. experimentally measurable quantities; **b.** theoretical model for the analysis of fluid flow.

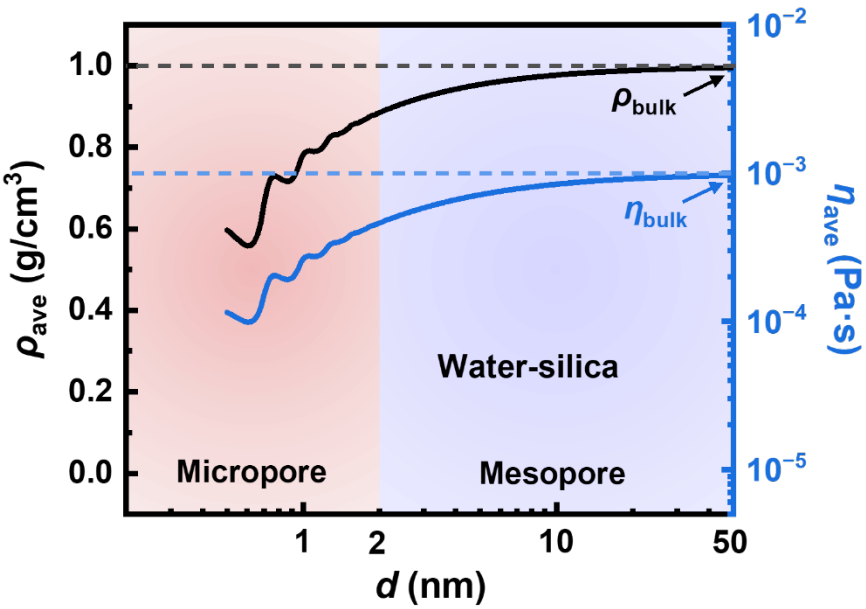

Fig. S13. The average density and viscosity of water in 0.5~50 nm silica

Table S10. The contact angle θ_c, wetting parameter α_w, slip length b of water on silica with different surface modifications.

Surfaces	θ_c (°)	α_w (/)	b (Å)
Silica (hydrophilic treated)	18.5	1.365	0.31
Silica (untreated)	73.5	0.537	2.01
Silica (hydrophobic treated)	82.5	0.468	2.65

The slip length of water on untreated silica was estimated by **Eq. (S43)**. The microscopic wetting parameters α_w were calculated by **Eq. (S44)**, then, the slip length of water on treated silica can be obtained according to **Eq. (S45)**.

S9. Theoretical design of hierarchical nanomaterials via re-derived Murray's law

From original Murray's law, the number of children pipes per parent pipe $N_{\mathrm{i,\ original}}$ is given by:

$$N_{i,original} = \frac{r_1^3}{r_2^3} = \frac{d_1^3}{d_2^3} \tag{S54}$$

For the hierarchically meso-microporous materials with d_1 = 10 nm, d_2 = 2 nm, $N_{\mathrm{i,original}}$ = 125. This value adjusts to $N_{\mathrm{i,\ modified}}$ = 25 according to **Eq. (S55)** when the modifying factor ξ_{Murray} = 4.98 (for water on untreated graphene, **Fig. 2e**).

$$N_{i,modified} = \frac{N_{i,original}}{\xi_{Murray}} = \frac{r_1^3}{r_2^3 \sqrt{\dfrac{\rho_{avg,i}\eta_{avg,0}\left(1+3b/r_0\right)\cdot\left(1+4b/r_i\right)^2}{\rho_{avg,0}\eta_{avg,i}\left(1+3b/r_i\right)\cdot\left(1+4b/r_0\right)^2}}} \tag{S55}$$

The mass transport resistances were calculated for N_{i} = 1~200. More specifically, parent pipe resistance R_1, children pipe resistance R_2, and their total resistance R_{hiera} can be obtained by **Eq. (S56)** to **(S58)**:

$$R_1 = R_{1,element} \cdot \frac{l_1}{A_1} = R_{1,element} \cdot \frac{l_1}{n_1 \pi r_1^2} \tag{S56}$$

$$R_2 = R_{2,element} \cdot \frac{l_2}{A_2} = R_{2,element} \cdot \frac{l_2}{n_2 \pi r_2^2} \tag{S57}$$

$$R_{hiera} = R_1 + R_2 \tag{S58}$$

where R_{element} is the elementary resistance per unit transport distance l_0 and area A_0, calculated by **Eq. (S46)**. n represents the number of parallel structural units (**Fig. 3a**), with $n_2 = N_{\mathrm{i}} \cdot n_1$. The structural parameters are constrained by:

$$V_{\mathrm{hiera}} = n_1 \pi r_1^2 l_1 + n_2 \pi r_2^2 l_2 \tag{S59}$$

$$S_{\mathrm{hiera}} = 2 n_1 \pi r_1 l_1 + 2 n_2 \pi r_2 l_2 \tag{S60}$$

where pore volume V_{hiera} and specific surface area S_{hiera} are defined as 1 m^3 and 1 m^2 to represent the unit quantity. Structural parameters (l_{i} and A_{i}) under the constraints of unit V and S vary with different N_{i}. As N_{i} increases, R_2 decreases due to more children tubes, while R_1 increases from reduced parallel structural units with larger surface area (**Fig. 3a**). This competition yields an extremum in R_{hiera}.

Case studies (varying d_1, d_2 and modifications, **Fig. S14**) consistently show minimized R_{hiera} when:

$$\frac{R_{1,element}l_1}{A_1} = \frac{R_{2,element}l_2}{A_2} \quad \text{or} \quad R_1 = R_2 \tag{S61}$$

This resistance matching principle (**Supplementary S4**) aligns with practical optimization strategies: reducing dominant resistance in series processes. Experimentally measurable resistances and emerging decoupling methods enable quantitative nanoscale Murray material design via **Eq. (S61)**.

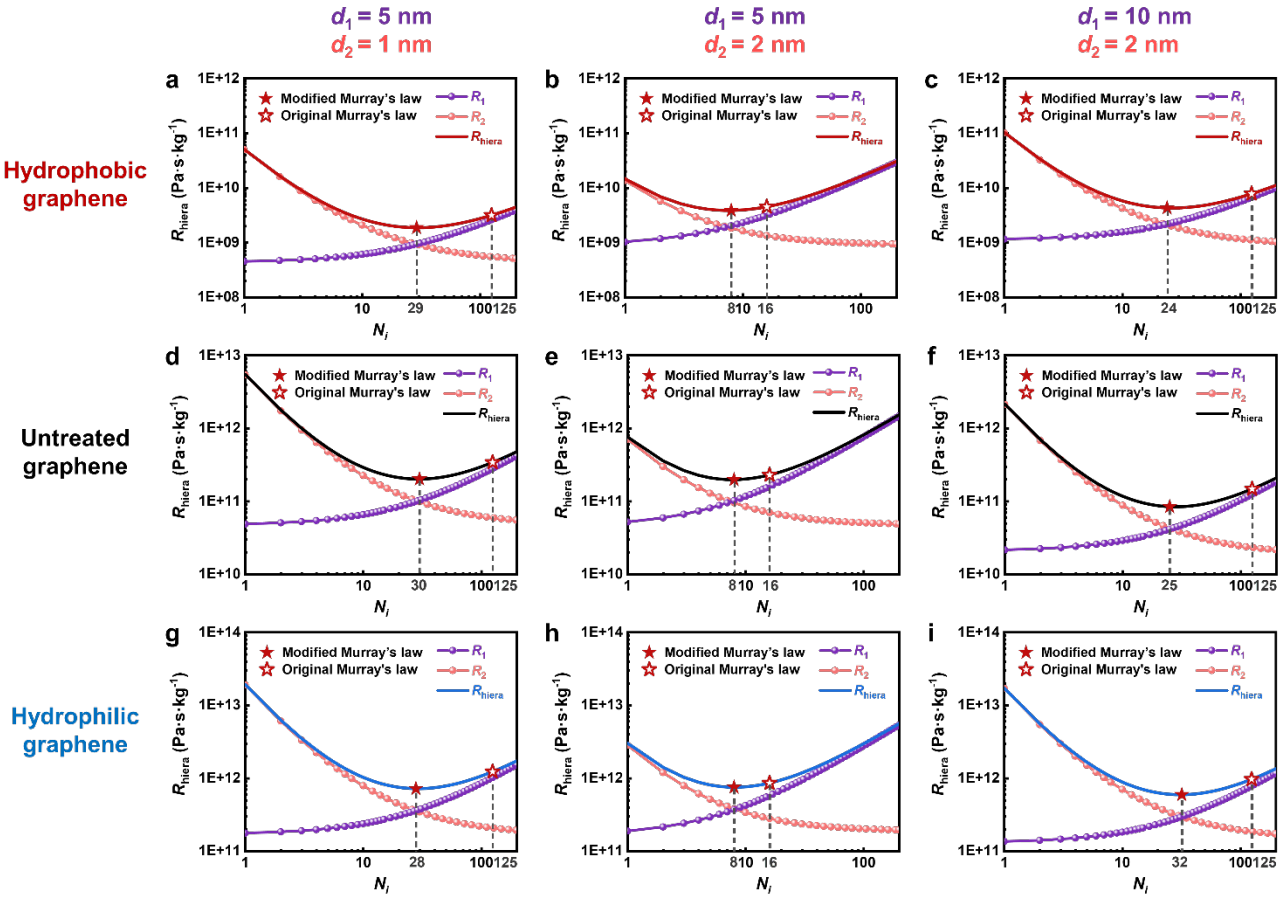

Fig S14. Mass transport resistance of water in hierarchical nanomaterial based on the theoretical design by original and modified Murray's law, containing varies cases with different pore sizes and surfaces.

S10. Hierarchically porous carbon in H_2O_2 synthesis

S10.1 Materials

Hierarchically porous carbons used in this work included commercial Cabot (Model Norit, Cabot Corporation) and self-made biomass skeleton carbon BioMC. BioMC was synthesized via a template-free approach using natural wood as a carbon precursor. The chemical used for hydrolysis treatment was NaOH (> 90%, Sinopharm Chemical Reagent Co., Ltd.).

BioMC- and Cabot-based catalysts were prepared as follows[6]: (1) Precursor preparation: $PdCl_2$ (Sigma-Aldrich Trading Co., Ltd.) was dissolved in 36 wt% HCl (Shanghai Lingfeng Chemical Reagent Co., Ltd) to achieve a nominal concentration of 0.05g Pd/mL; (2) Impregnation treatment: BioMC/Cabot supports were stirred with precursor solutions for 6 h; (3) Drying: filtered precursors were freeze-dried at -55 ℃ to remove water; (4) Heat treatment: Samples were roasted at 300 ℃ in static air to synthesize 1 wt% Pd/BioMC and 1 wt% Pd/Cabot.

According to the pore size distributions (**Fig. S15**), BioMC and Cabot had 6nm mesopores and 1nm micropores on average. In addition, The Brunauer–Emmett–Teller (BET)-specific surface area and pore structure parameters of different porous carbons were listed in **Table S11**.

S10.2 Hierarchical carbon-based catalyst testing

Direct synthesis of hydrogen peroxide (H_2O_2) from H_2 and O_2 is a typical heterogeneous reaction, which is used to test the BioMC-based and Cabot-based catalysts. There is a trade-off between selectivity and productivity of H_2O_2 because the intermediate product H_2O_2 is less favorable than the end-product H_2O thermodynamically. Therefore, the formation of by-product H_2O can be effectively inhibited due to the fast transport of H_2O_2 in the porous catalyst support, and the excellent mass transfer capability of reactants H_2 and O_2 can improve the reaction conversion rate. In summary, the optimal mass transport of reactants in nanomaterials is expected to break the selectivity- productivity trade-off in H_2O_2 synthesis.

Catalytic testing was completed in a self-made gas-liquid-solid three-phase glass batch reactor[6]. The reaction solvent was composed of 48 mL ethanol (99.9 wt%) and 0.305 mL concentrated sulfuric acid (98 wt%, Shanghai Lingfeng Chemical Reagent Co., Ltd). The reaction atmosphere was composed of

H_2, O_2, and N_2, with flow rates of 7.2, 28.8, and 12 mL/min respectively. They were bubbled into the liquid phase after passing through the sand core at the reactor bottom, and the gas inlet temperature was adjusted via a temperature control device. The reaction was completed under a conventional condition with 0.1 MPa and 10 °C. After adding 40 mg catalysts into the reactor, timing was started. The H_2 concentration in the tail gas was regularly detected by gas chromatography (Model SP-3420A, Beifen-Ruili Instrument Co., Ltd., China Beijing) to calculate H_2 conversion (X_{H2}). Selectivity (S) and productivity (P) of H_2O_2 were calculated based on its concentration in the reaction solvent, determined by titanium oxysulfate colorimetry.

1 wt% Pd/BioMC outperformed 1 wt% Pd/Cabot in conversion, selectivity, and productivity (**Fig. S16**). However, since both catalysts were prepared identically, the difference in performance was attributed solely to the transport capacity of catalytic supports.

S10.3 Measurement of mass transport resistance via microcalorimetry

Microcalorimetry experiments were developed to measure mass transport structural parameters. in nanomaterials. Specifically, these experiments involved adding a controlled amount of H_2O_2 to the solution with porous carbon. The resulting heat effect (accurately measured by high-precision calorimetry.) was correlated with mass transport flux (J). The deviation of H_2O_2 concentration from equilibrium over time was quantified as the driving force (X), and mass transport resistance (R) was derived using linear non-equilibrium thermodynamics as **Eq. (S20)**.

Calorimetric titration experiments were performed using a TAM Air isothermal microcalorimeter (TA Instruments, USA). The parallel dual-chamber measurement channels, i.e., the measurement channel and the reference channel, were used during the measurement. In the measurement channel, 30 mg of porous carbon was dispersed in 2 mL pure water within a 20 mL ampoule. A Hamilton syringe containing 2 mL aqueous H_2O_2 was positioned above the ampoule with automatic agitation. The reference channel used pure water in the syringe to eliminate external temperature effects.

Since the measurable H_2O_2 mass transport resistance in aqueous solution cannot be directly extended to reactant behavior in ethanol solution (used in H_2O_2 synthesis), geometric parameters (mass transport distance l and area A) were analyzed. For fixed nanomaterial structures, resistance for varies fluids can

be predicted via theoretically calculated elementary resistance R_{element}. A working equation was established to solve geometric structures via microcalorimetry data:

$$R_{hiera} = R_{meso,element} \cdot \frac{l_{meso}}{A_{meso}} + R_{micro,element} \cdot \frac{l_{micro}}{A_{micro}} + R_{s,element} \cdot \frac{1}{a_p} \quad \text{(S62)}$$

By constraining l and A with pore volume V ($A=V/l$), only two structural variables for mesopores and micropores remained. Additionally, $R_{\text{s,element}}$ (defined as the elementary resistance of quasi reaction) differed depending on Pd presence, yielding four total variables. **Eq. (S62)** can be used to establish four different equations for four types of porous carbon (BioMC, Cabot, 1 wt% Pd/BioMC, and 1 wt% Pd/Cabot), followed by solving them simultaneously. The solved mass transport geometric parameters of four materials were listed in **Table S12**. Mass transport resistances for BioMC and Cabot, calculated via R_{element} (**Fig. S17**) and **Eq. (S62)**, were listed in **Table S13**.

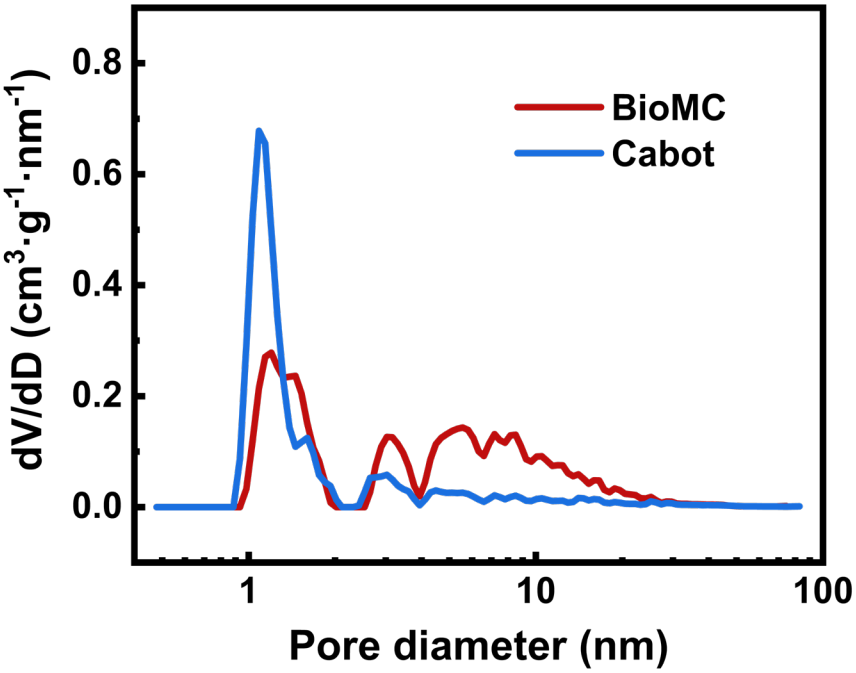

Fig S15. The pore size distributions of BioMC and Cabot.

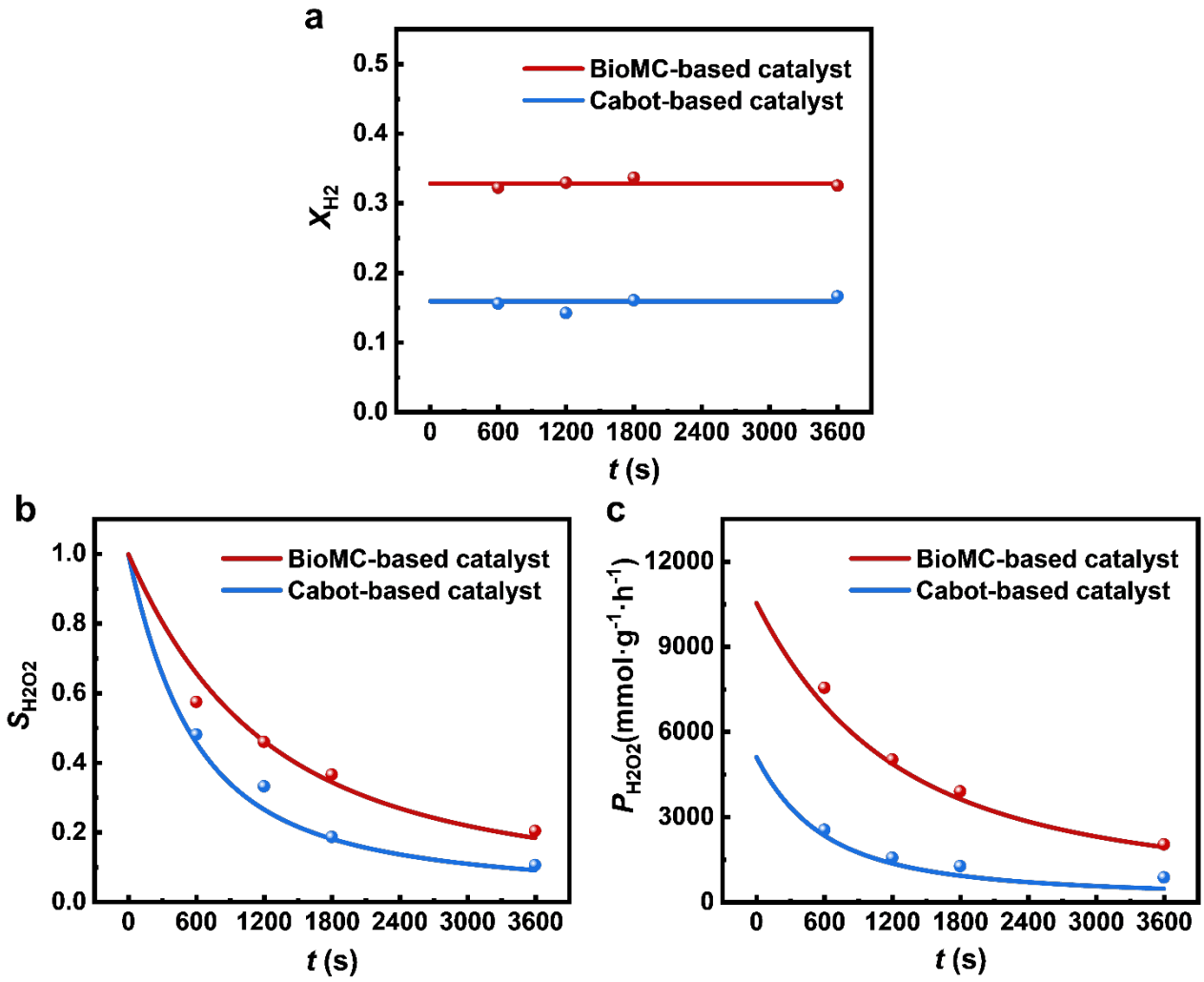

Fig S16. The reaction performances of BioMC-based and Cabot-based catalysts: **a.** conversion efficiency of H_2; **b.** selectivity of H_2O_2, **c.** productivity of H_2O_2. The dots in the figure represent experimental values, and the solid lines represent the predicted values of reaction kinetics model.

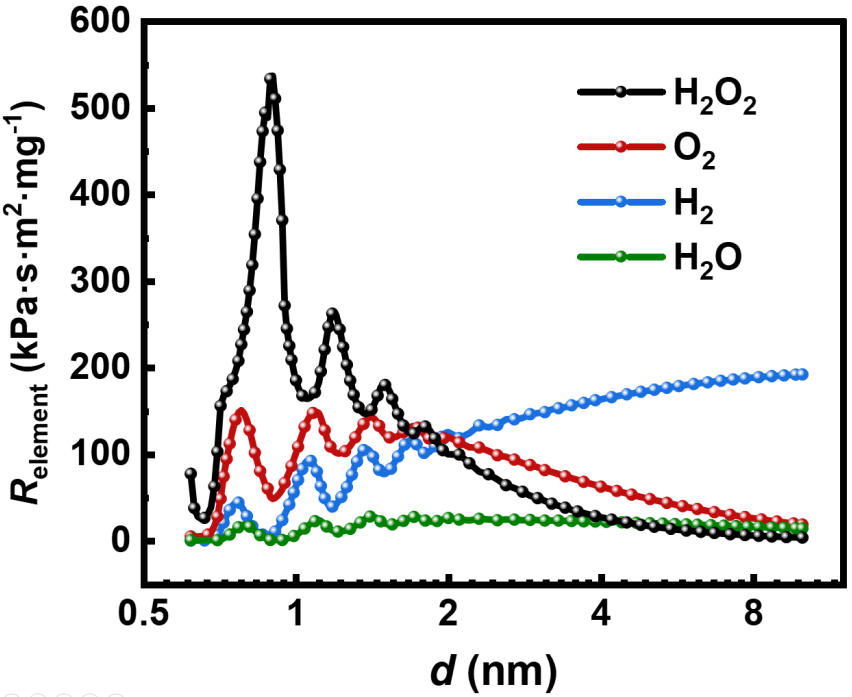

Fig S17. The elementary mass transport resistance of H_2O_2, H_2, O_2, and H_2O in carbon channels with different pore sizes *d*

Table S11. Pore structures of hierarchically porous carbons.

Sample	BET specific surface area	Micro-area	Meso-area	Pore volume	Micropore volume	Mesopore volume
	m^2/g	m^2/g	m^2/g	cm^3/g	cm^3/g	cm^3/g
Cabot	702.6	549.6	153.0	0.65	0.24	0.41
BioMC	861.5	310.4	551.1	1.72	0.16	1.56
1 wt% Pd/Cabot	794.5	654.6	139.9	0.71	0.29	0.42
1 wt% Pd/BioMC	925.3	356.5	568.8	1.80	0.18	1.62

Table S12. Geometric parameters of four porous carbons.

Porous carbon	n_{meso} (g^{-1})	n_{micro} (g^{-1})	A_{meso} ($m^2 \cdot g^{-1}$)	A_{micro} ($m^2 \cdot g^{-1}$)	l_{meso} (m)	l_{micro} (m)
Cabot	7.03×10^{11}	3.53×10^{13}	1.99×10^{-5}	2.77×10^{-5}	0.0053	0.0022
BioMC	2.64×10^{12}	2.35×10^{13}	7.47×10^{-5}	1.84×10^{-5}		
1 wt% Pd/Cabot	7.13×10^{11}	4.20×10^{13}	2.02×10^{-5}	3.21×10^{-5}		
1 wt% Pd/BioMC	2.62×10^{12}	2.55×10^{13}	7.41×10^{-5}	1.95×10^{-5}		

In **Table S12**, n_{meso} and n_{micro} represent the numbers of parallel mesoporous and microporous channels per gram of catalyst, respectively. All geometric parameters listed here are statistical average values due to the inherent structural non-uniformity. Therefore, future research on Murray's law should prioritize uniform construction of hierarchical pores to advance the theory.

Table S14. The mass transport resistances of reactants in BioMC and Cabot. R_1 and R_2 represented the mass transport resistance of parent and children tubes, respectively, and R_{hiera} was the total mass transport resistance.

Fluids	Cabot (kPa·m^3·s/mg)			BioMC (kPa·m^3·s/mg)		
	R_1	R_2	R_{hiera}	R_1	R_2	R_{hiera}
H_2	43.3	7.7	51.0	11.9	12.2	24.1
O_2	5.3	1.3	6.6	1.4	1.8	3.2
H_2O_2	28.0	6.4	34.4	7.4	9.7	17.1
H_2O	4.3	0.1	4.4	1.1	0.1	1.2

S11. Mass transport of guest molecules in nanoporous crystalline materials

S11.1 Materials

All data on SAPO-34 zeolites mentioned in this work are sourced from published articles by Mao Ye. et al [33, 34, 35], including SAPO-0.05, SAPO-0.5, SAPO-1.0 (Si-0.05), SAPO-1.0 (Si-0.08), SAPO-1.0 (Si-0.10), SAPO-1.0 (Si-0.16), SAPO-3.5, and SAPO-8. SAPO-34 zeolites with different crystal sizes exhibit similar cubic morphology. For example, SAPO-0.5 has an average crystal size of ~ 0.5 μm, SAPO-1.0 of ~ 1 μm, and so on. The values in parentheses in **Fig. 4d** represent the chemical composition of SAPO-34 zeolites. Detailed compositions were listed in **Table S15**.

S11.2 Surface permeability and intracrystalline diffusion coefficient

Surface barriers and intracrystalline diffusion dominate guest molecules transport in nanoporous crystalline materials. The lack of methods to separately quantify these mechanisms hinders rational design and efficient application of nanoporous materials. Mao Ye. et al.[35] proposed a decoupling method to measure surface permeability α and intracrystalline diffusion coefficient D. The mass transport parameters of propane in SAPO-34 zeolites were listed in **Table S16**, where L is the ratio of the characteristic time of intracrystalline diffusion to that of surface barriers; l is the characteristic length of mass transport.

S11.3 Mass transport resistance of surface permeability (parent tubes) and intracrystalline diffusion (children tubes)

Effective diffusivity can be expressed as resistances (due to their additive property), combining surface permeability and intracrystalline diffusivity[36]:

$$\frac{l}{D_{eff}} = \frac{l}{D} + \frac{3}{\alpha} \quad \text{or} \quad R_{total} = R_{\text{diff}} + R_{\text{perm}} \tag{S63}$$

Based on this, **Table S16** is converted to resistance form in **Table S17**.

Table S15. Chemical composition of SAPO-34 zeolites [35].

Sample	Integral composition
SAPO-34-0.05	$(Si_{0.155}Al_{0.421}P_{0.424})O_2$
SAPO-34-0.5	$(Si_{0.124}Al_{0.463}P_{0.413})O_2$
SAPO-34-0.1 (0.16)	$(Si_{0.167}Al_{0.399}P_{0.434})O_2$
SAPO-34-0.1 (0.10)	$(Si_{0.103}Al_{0.486}P_{0.412})O_2$
SAPO-34-0.1 (0.08)	$(Si_{0.087}Al_{0.495}P_{0.420})O_2$
SAPO-34-0.1 (0.05)	$(Si_{0.058}Al_{0.418}P_{0.524})O_2$
SAPO-34-3.5	$(Si_{0.079}Al_{0.492}P_{0.429})O_2$
SAPO-34-8	$(Si_{0.088}Al_{0.485}P_{0.428})O_2$

Table S16. The surface permeability α, intracrystalline diffusivity D, and effective diffusivity D_{eff} of propane in SAPO-34 zeolites with varying crystal size and Si content at 313 K [35].

Sample	α (m/s)	D (m^2/s)	D_{eff} (m^2/s)	$L=\alpha l/D$
SAPO-0.05	2.21×10^{-10}	1.05×10^{-16}	8.99×10^{-19}	0.03
SAPO-0.5	1.69×10^{-9}	1.25×10^{-16}	2.82×10^{-17}	1.67
SAPO-0.1 (0.16)	1.37×10^{-9}	8.66×10^{-17}	5.84×10^{-17}	6.19
SAPO-0.1 (0.10)	2.03×10^{-9}	7.50×10^{-17}	5.17×10^{-17}	6.67
SAPO-0.1 (0.08)	2.53×10^{-9}	2.35×10^{-16}	1.10×10^{-16}	2.65
SAPO-0.1 (0.05)	3.07×10^{-9}	1.98×10^{-16}	1.11×10^{-16}	3.82
SAPO-3.5	6.18×10^{-9}	1.23×10^{-16}	1.15×10^{-16}	43.30
SAPO-8	5.74×10^{-9}	1.63×10^{-16}	1.56×10^{-16}	69.39

Table S17. The resistance of surface permeability R_{perm}, intracrystalline diffusivity R_{diff}, and total mass transport resistance R_{total} of propane in SAPO-34 zeolites with varying crystal size and Si content at 313 K.

Sample	R_{perm} (s/m)	R_{diff} (s/m)	R_{total} (s/m)	R_{perm}/R_{diff}
SAPO-0.05	1.36×10^{10}	1.36×10^{8}	1.37×10^{10}	100.00
SAPO-0.5	1.78×10^{9}	9.88×10^{8}	2.76×10^{9}	1.79
SAPO-0.1 (0.16)	2.19×10^{9}	4.52×10^{9}	6.71×10^{9}	0.48
SAPO-0.1 (0.10)	1.48×10^{9}	3.29×10^{9}	4.76×10^{9}	0.45
SAPO-0.1 (0.08)	1.19×10^{9}	1.05×10^{9}	2.23×10^{9}	1.13
SAPO-0.1 (0.05)	9.77×10^{8}	1.24×10^{9}	2.22×10^{9}	0.79
SAPO-3.5	4.85×10^{8}	7.01×10^{9}	7.49×10^{9}	0.07
SAPO-8	5.23×10^{8}	1.21×10^{10}	1.26×10^{10}	0.04

Supplementary references

1. Demirel YA, Sandler SI. Nonequilibrium thermodynamics in engineering and science. *Journal of Physical Chemistry B* **108**, 31-43 (2004).

2. Onsager L. Reciprocal Relations in Irreversible Processes. I. *Physical Review* **37**, 405-426 (1931).

3. Onsager L. Reciprocal Relations in Irreversible Processes. II. *Physical Review* **38**, 2265-2279 (1931).

4. Wang SS, Chen JJ, Li LC, Huang LL, Lu XH, Zuo SL. Mass transfer behavior of methane in porous carbon materials. *AIChE Journal* **68**, e17521 (2021).

5. Xie WL, Ji XY, Feng X, Lu XH. Mass-transfer rate enhancement for CO_2 separation by ionic liquids: Theoretical study on the mechanism. *AIChE Journal* **61**, 4437-4444 (2015).

6. Cao J*, et al.* Heterogeneous consecutive reaction kinetics of direct oxidation of H_2 to H_2O_2: Effect and regulation of confined mass transfer. *Chemical Engineering Journal* **455**, 140111 (2023).

7. Shan XD, Wang M, Guo ZY. Geometry optimization of self-similar transport network. *Mathematical Problems in Engineering* **2011**, 421526 (2011).

8. Ma RZ*, et al.* Atomic imaging of the edge structure and growth of a two-dimensional hexagonal ice. *Nature* **577**, 60-63 (2020).

9. Frink LJD, Thompson A, Salinger AG. Applying molecular theory to steady-state diffusing systems. *Journal of Chemical Physics* **112**, 7564-7571 (2000).

10. Shen G, Ji X, Lu X. A hybrid perturbed-chain SAFT density functional theory for representing fluid behavior in nanopores. *The Journal of Chemical Physics* **138**, 194705 (2013).

11. Shen G, Ji X, Öberg S, Lu X. A hybrid perturbed-chain SAFT density functional theory for representing fluid behavior in nanopores: Mixtures. *The Journal of Chemical Physics* **139**, 194705 (2013).

12. Chen X*, et al.* Accurate prediction of solvent flux in sub–1-nm slit-pore nanosheet membranes. *Science Advances* **10**, eadl1455 (2024).

13. Zuo ZD, Lu XH, Ji XY. Modeling self-diffusion coefficients of ionic liquids using ePC-SAFT and FVT combined with the Einstein relation. *AICHE Journal* **70**, e18468 (2024).

14. Zuo Z, Lu X, Ji X. Modeling self-diffusion coefficient and viscosity of chain-like fluids based on ePC-SAFT. *Journal of Chemical & Engineering Data* **69**, 348-362 (2024).

15. Zhu Y, Lu XH, Zhou J, Wang YR, Shi J. Prediction of diffusion coefficients for gas, liquid and supercritical fluid: application to pure real fluids and infinite dilute binary solutions based on the simulation of Lennard-Jones fluid. *Fluid Phase Equilibria* **194**, 1141-1159 (2002).

16. Pan XL*, et al.* Modeling of Alcohol/Water Separation in Graphene-Based Membranes: The Roles of Interfacial Adsorption and the Effective Transfer Path. *Industrial & Engineering Chemistry Research* **63**, 6399-6410 (2024).

17. Zhao S, Hu Y, Yu X, Liu Y, Bai Z-S, Liu H. Surface wettability effect on fluid transport in nanoscale slit pores. *AIChE Journal* **63**, 1704-1714 (2017).

18. Gubbins KE, Long Y, Śliwinska-Bartkowiak M. Thermodynamics of confined nano-phases. *The Journal of Chemical Thermodynamics* **74**, 169-183 (2014).

19. Barrat JL, Bocquet L. Influence of wetting properties on hydrodynamic boundary conditions at a fluid/solid interface. *Faraday Discussions* **112**, 119-127 (1999).

20. Wang Y, Xu J, Yang C. Fluid inhomogeneity within nanoslits and deviation from Hagen–Poiseuille flow. *AIChE Journal* **63**, 834-842 (2017).

21. Celebi AT, Nguyen CT, Hartkamp R, Beskok A. The role of water models in the prediction of slip length of water in graphene nanochannels. *Journal of Chemical Physics* **151**, 174705 (2019).

22. Kumar Kannam S, Todd BD, Hansen JS, Daivis PJ. Slip length of water on graphene: Limitations of non-equilibrium molecular dynamics simulations. *The Journal of Chemical Physics* **136**, 024705 (2012).

23. Maali A, Bhushan B. Measurement of slip length on superhydrophobic surfaces. *Philosophical Transactions of the Royal Society A* **370**, 2304-2320 (2012).

24. Joshi RK*, et al.* Precise and ultrafast molecular sieving through graphene oxide membranes. *Science* **343**, 752-754 (2014).

25. Mouterde T*, et al.* Molecular streaming and its voltage control in ångström-scale channels. *Nature* **567**, 87-90 (2019).

26. Radha B*, et al.* Molecular transport through capillaries made with atomic-scale precision. *Nature* **538**, 222-225 (2016).

27. Xie Q*, et al.* Fast water transport in graphene nanofluidic channels. *Nature Nanotechnology* **13**, 238-245 (2018).

28. Bocquet L, Charlaix E. Nanofluidics, from bulk to interfaces. *Chemical Society Reviews* **39**, 1073-1095 (2010).

29. Chen Z, Dong L, Yang D, Lu H. Superhydrophobic Graphene-Based Materials: Surface Construction and Functional Applications. *Advanced Materials* **25**, 5352-5359 (2013).

30. Ito S, Seto Y, Kumaki J, Nakagawa M. Macromolecular Chain Structures of Atactic Poly(methyl methacrylate) Visualized on Hydrophilized Graphene Surfaces by Atomic Force Microscopy. *Chemistry Letters* **50**, 1403-1406 (2021).

31. Li B*, et al.* A multi-scale architecture for multi-scale simulation and its application to gas-solid flows. *Particuology* **15**, 160-169 (2014).

32. An R, Huang LL, Mineart KP, Dong YH, Spontak RJ, Gubbins KE. Adhesion and friction in polymer films on solid substrates: conformal sites analysis and corresponding surface measurements. *Soft Matter* **13**, 3492-3505 (2017).

33. Gao M, Li H, Ye M, Liu Z. An approach for predicting intracrystalline diffusivities and adsorption entropies in nanoporous crystalline materials. *AIChE Journal* **66**, e16991 (2020).

34. Peng S, Gao M, Li H, Yang M, Ye M, Liu Z. Control of Surface Barriers in Mass Transfer to Modulate Methanol-to-Olefins Reaction over SAPO-34 Zeolites. *Angew Chem Int Ed Engl* **59**, 21945-21948 (2020).

35. Gao M*, et al.* Direct quantification of surface barriers for mass transfer in nanoporous crystalline materials. *Communications Chemistry* **2**, 43 (2019).

36. Saint Remi JC*, et al.* The role of crystal diversity in understanding mass transfer in nanoporous materials. *Nature Materials* **15**, 401-406 (2016).